

Inverse problem regularization with hierarchical variational autoencoders

Jean Prost

Univ. Bordeaux, CNRS, Bordeaux INP
IMB, UMR 5251, F-33400 Talence, France

jean.prost@math.u-bordeaux.fr

Andrés Almansa

Université Paris Cité, CNRS
MAP5, UMR 8145

andres.almansa@parisdescartes.fr

Antoine Houdard

Ubisoft La Forge
Bordeaux

antoine.houdard@ubisoft.com

Nicolas Papadakis

Univ. Bordeaux, CNRS, Bordeaux INP
IMB, UMR 5251, F-33400 Talence, France

nicolas.papadakis@math.u-bordeaux.fr

Abstract

In this paper, we propose to regularize ill-posed inverse problems using a deep hierarchical variational autoencoder (HVAE) as an image prior. The proposed method synthesizes the advantages of i) denoiser-based Plug & Play approaches and ii) generative model based approaches to inverse problems. First, we exploit VAE properties to design an efficient algorithm that benefits from convergence guarantees of Plug-and-Play (PnP) methods. Second, our approach is not restricted to specialized datasets and the proposed PnP-HVAE model is able to solve image restoration problems on natural images of any size. Our experiments show that the proposed PnP-HVAE method is competitive with both SOTA denoiser-based PnP approaches, and other SOTA restoration methods based on generative models. The code for this project is available at <https://github.com/jprost76/PnP-HVAE>.

1. Introduction

In this work, we study linear inverse problems

$$\mathbf{y} = \mathbf{A}\mathbf{x} + \epsilon \quad (1)$$

in which $\mathbf{y} \in \mathbb{R}^m$ is the degraded observation, $\mathbf{x} \in \mathbb{R}^d$ the original signal we wish to retrieve, $\mathbf{A} \in \mathbb{R}^{m \times d}$ is an observation matrix and $\epsilon \sim \mathcal{N}(0, \sigma^2 \mathbf{I})$ is an additive Gaussian noise. Many image restoration tasks can be formulated as (1), including deblurring, super-resolution or inpainting.

With the development of deep learning in computer vision, image restoration have known significant progress. The most straight-forward way to exploit deep learning for solving image inverse problems is to train a neural network to map degraded images to their clean version in a supervised fashion. However, this type of approach requires a

large amount of training data, and it lacks flexibility, as one network is needed for each different inverse problem.

An alternate approach is to use deep latent variable generative models such as GANs or VAEs and to compute the Maximum-a-Posterior (MAP) estimator in the latent space:

$$\hat{\mathbf{z}} = \arg \max_{\mathbf{z}} \log p(\mathbf{y}|\mathbf{G}(\mathbf{z})) + \log p(\mathbf{z}), \quad (2)$$

where \mathbf{z} is the latent variable and \mathbf{G} is the generative network [4, 34]. In (2) the likelihood $p(\mathbf{y}|\mathbf{G}(\mathbf{z}))$ is related to the forward model (1), and $p(\mathbf{z})$ corresponds to the prior distribution over the latent space. After solving (2), the solution of the inverse problem is defined as $\hat{\mathbf{x}} = \mathbf{G}(\hat{\mathbf{z}})$. The latent optimization methods (2) provide high-quality solutions that are guaranteed to be in the range of a generative network. However, this implies highly non-convex problems (2) due to the complexity of the generator and the obtained solutions may lack of consistency with the degraded observation [47]. Although the convergence of latent optimization algorithms has been studied in the literature, existing convergence guarantees are either restricted to specific settings, or rely on assumptions that are hard to verify.

In this work, we propose an algorithm that exploits the strong prior of a deep generative model while providing realistic convergence guarantees. We consider a specific type of deep generative model, the hierarchical variational autoencoder (HVAE). HVAE gives state-of-the-art results on image generation benchmarks [53, 6, 15, 31], and provides an encoder that will be key in the design of our proposed method.

As the HVAE model differs significantly from the architecture of concurrent models, it is necessary to design algorithms adapted to their specific structure. The latent space dimension of HVAE is significantly higher than the image dimension. Hence, constraining the solution to lie in the image of the generator is not sufficient enough to regularize

inverse problems. Indeed, it has been observed that HVAEs can perfectly reconstruct out-of-domain images [14]. Consequently, we propose to constrain the latent variable of the solution to lie in the high probability area of the HVAE prior distribution. This can be done efficiently by controlling the variance of the prior over the latent variables.

The common practice of optimizing the latent variables of the generative model with backpropagation is impractical due to the high dimensionality of the hierarchical latent space. Instead, we exploit the HVAE encoder to define an alternating algorithm [11] to optimize the joint distribution over the image and its latent variable

To derive convergence guarantees for our algorithm, we show that it can be reformulated as a Plug-and-Play (PnP) method [54], which alternates between an application of the proximal operator of the data-fidelity term, and a reconstruction by the HVAE. Under this perspective, we give sufficient conditions to ensure the convergence of our method, and we provide an explicit characterization of the fixed-point of the iterations. Motivated by the parallel with PnP methods, we name our method PnP-HVAE.

1.1. Contributions and outline

In this work, we introduce PnP-HVAE, a method for regularizing image restoration problems with a hierarchical variational autoencoder. Our approach exploits the expressiveness of a deep HVAE generative model and its capacity to provide a strong prior on specialized datasets, as well as convergence guarantees of Plug-and-Play methods and their ability to deal with natural images of any size. After a review of related works (section 2) and of the background on HVAEs (section 3), our contributions are the following.

- In section 4, we introduce PnP-HVAE, an algorithm to solve inverse problems with a HVAE prior. PnP-HVAE optimizes a joint posterior on image and latent variables without backpropagation through the generative network. It can be viewed as a generalization of JPMAP [11] to hierarchical VAEs, with additional control of the regularization.
- In section 5, we demonstrate the convergence of PnP-HVAE under hypotheses on the autoencoder reconstruction. Numerical experiments illustrate that the technical hypotheses are empirically met on noisy images with our proposed architecture. We also exhibit the better convergence properties of our alternate algorithm with respect to the use of Adam for optimizing the joint posterior objective.
- In section 6, we demonstrate the effectiveness of PnP-HVAE through image restoration experiments and comparisons on (i) faces images using the pre-trained VDVAE model from [6]; and (ii) natural images using the proposed PatchVDVAE architecture trained on natural image patches.

2. Related works

CNN methods for regularizing inverse problems can be classified in two categories: regularization with denoisers (Plug-and-Play) and regularization with generative models.

2.1. Plug-and-Play methods

Plug-and-Play (PnP) and RED methods [54, 43] make use of a (deep) denoising method as a proxy to encode the local information over the prior distribution. The denoiser is plugged in an optimization algorithm such as Half-Quadratic Splitting or ADMM in order to solve the inverse problem. PnP algorithms come with theoretical convergence guarantees by imposing certain conditions on the denoiser network [45, 37, 19]. These approaches provide state-of-the-art results on a wide variety of image modality thanks to the excellent performance of the currently available deep denoiser architectures [55]. However, PnP methods are only implicitly related to a probabilistic model, and they provide limited performance for challenging structured problems such as the inpainting of large occlusions.

2.2. Deep generative models for inverse problems

Generative models represent an explicit image prior that can be used to regularize ill-posed inverse problems [4, 26, 34, 8, 35, 36, 51]. They are latent variable models parametrized by neural networks, optimized to fit a training data distribution [25, 12, 10, 16].

Convergence issues. Regularization with generative models (2) involves highly non-convex optimization over latent variables [4, 34, 35]. The convergence guarantees of existing methods remain to be established [48, 40, 17].

Convergent methods have only been proposed for restricted uses cases. In compressed sensing problems with Gaussian measurement matrices, one can show that the objective function has a few critical points and design an algorithm to find the global optimum [13, 18]. With a prior given by a VAE, and under technical hypothesis on the encoder and the VAE architecture, the Joint Posterior Maximization with Autoencoding Prior (JPMAP) framework of [11] converges toward a minimizer of the joint posterior $p(x, z|y)$ of the image x and latent z given the observation y . JPMAP is nevertheless only designed for VAEs of limited expressiveness, with a simple fixed Gaussian prior distribution over the latent space. This makes it impossible to use this approach for anything other than toy examples.

Genericity issues. When a highly structured dataset with fixed image size is available (e.g. face images [20]), deep generative models produce image restorations of impressive quality for severely ill-posed problems, such as super-resolution with huge upscaling factors.

For natural images, deep priors have been improved by normalizing flows [41, 10], GANs [12], score-based [52]

and diffusion models [16, 47, 46]. Note that the use of diffusion models in PnP is still based on approximations [50, 7], assumptions [22, 33] or empirical algorithms [30].

While GAN models were considered SOTA, modern hierarchical VAE (HVAE) architectures were shown to display quality on par with GANs [6, 53], while being able to perfectly reconstruct out-of-domain images [14].

Integrating HVAE in a convergent scheme for natural image restoration of any size raises several theoretical and methodological challenges, as the image model of HVAE is the push-forward of a *causal cascade of latent distributions*.

3. Background on variational autoencoders

This work exploits the capacity of HVAEs to model complex image distributions [6, 53]. We review the properties of the loss function used to train a VAE (section 3.1), then we detail the generalization of VAE to hierarchical VAE (section 3.2), and present the temperature scaling approach to monitor the quality of generated images (section 3.3).

3.1. VAE training

Variational autoencoders (VAE) have been introduced in [25] to model complex data distributions. VAEs are trained to fit a parametric probability distribution in the form of a latent variable model:

$$p_\theta(\mathbf{x}) = \int p_\theta(\mathbf{x}|\mathbf{z})p_\theta(\mathbf{z})d\mathbf{z}, \quad (3)$$

where $p_\theta(\mathbf{x}|\mathbf{z})$ is a probabilistic decoder, and $p_\theta(\mathbf{z})$ corresponds to the prior distribution over the model latent variable \mathbf{z} . A VAE is also composed of a probabilistic encoder $q_\phi(\mathbf{z}|\mathbf{x})$, whose role is to approximate the posterior of the latent model $p_\theta(\mathbf{z}|\mathbf{x})$, which is usually intractable.

The generative model parameters $\theta \in \Theta$ and the approximate posterior parameters $\phi \in \Phi$ of a VAE are jointly trained by maximizing the evidence lower bound (ELBO) [25, 42] on a training data distribution $p_{\text{data}}(\mathbf{x})$.

$$\mathcal{L}(\mathbf{x}; \theta, \phi) = \mathbb{E}_{q_\phi(\mathbf{z}|\mathbf{x})}[\log p_\theta(\mathbf{x}|\mathbf{z})] - \text{KL}(q_\phi(\mathbf{z}|\mathbf{x})||p_\theta(\mathbf{z})). \quad (4)$$

The ELBO expectation on $p_{\text{data}}(\mathbf{x})$ is upper-bounded by the negative entropy of the data distribution, and, when the upper-bound is reached we have that [56]:

$$\text{KL}(p_{\text{data}}(\mathbf{x})q_\phi(\mathbf{z}|\mathbf{x})||p_\theta(\mathbf{x})p_\theta(\mathbf{z}|\mathbf{x})) = 0. \quad (5)$$

3.2. Hierarchical variational autoencoders

The ability of hierarchical VAEs to model complex distributions is due to their hierarchical structure imposed in the latent space. The latent variable of HVAE is partitioned into L subgroups $\mathbf{z} = (\mathbf{z}_0, \mathbf{z}_1, \dots, \mathbf{z}_{L-1})$, and the prior

and the encoder are respectively defined as:

$$p_\theta(\mathbf{z}) = \prod_{l=1}^{L-1} p_\theta(\mathbf{z}_l|\mathbf{z}_{<l})p_\theta(\mathbf{z}_0) \quad (6)$$

$$q_\phi(\mathbf{z}|\mathbf{x}) = \prod_{l=1}^{L-1} q_\phi(\mathbf{z}_l|\mathbf{z}_{<l}, \mathbf{x})q_\phi(\mathbf{z}_0|\mathbf{x}), \quad (7)$$

We consider a specific class of HVAEs with Gaussian conditional distributions for the encoder and the decoder

$$\begin{cases} p_\theta(\mathbf{z}_l|\mathbf{z}_{<l}) = \mathcal{N}(\mathbf{z}_l; \mu_{\theta,l}(\mathbf{z}_{<l}), \Sigma_{\theta,l}(\mathbf{z}_{<l})) \\ q_\phi(\mathbf{z}_l|\mathbf{z}_{<l}, \mathbf{x}) = \mathcal{N}(\mathbf{z}_l; \mu_{\phi,l}(\mathbf{z}_{<l}, \mathbf{x}), \Sigma_{\phi,l}(\mathbf{z}_{<l}, \mathbf{x})), \end{cases} \quad (8)$$

where $\mu_{\theta,0}$ and $\Sigma_{\theta,0}$ can either be trainable or non-trainable constants, and the remaining mean vectors ($\mu_{\theta,l}$, and $\mu_{\phi,l}$, for $l > 0$) and covariance matrices ($\Sigma_{\theta,l}$ and $\Sigma_{\phi,l}$, for $l > 0$) are parametrized by neural networks.¹ In this work, we consider models with a Gaussian decoder:

$$p_\theta(\mathbf{x}|\mathbf{z}) = \mathcal{N}(\mathbf{x}; \mu_\theta(\mathbf{z}), \gamma^2 I). \quad (9)$$

3.3. Temperature scaling

As demonstrated in [53, 6], sampling the latent variables \mathbf{z}_l from a prior with reduced temperature improves the visual quality of the generated images from the VAE. In practice, this is done by multiplying the covariance matrix of the Gaussian distribution $p_\theta(\mathbf{z}_l|\mathbf{z}_{<l})$ by a factor $\tau_l < 1$. This factor τ_l is called temperature because of its link to statistical physics. Reducing the temperature of the priors amounts to defining the auxiliary model:

$$p_{\theta,\tau}(\mathbf{z}_0, \dots, \mathbf{z}_{L-1}, \mathbf{x}) = \prod_{l=0}^{L-1} \frac{p_\theta(\mathbf{z}_l|\mathbf{z}_{<l})^{\frac{1}{\tau_l^2}}}{Z_l} p_\theta(\mathbf{x}|\mathbf{z}_{<L}), \quad (10)$$

where $\tau := (\tau_0, \dots, \tau_{L-1})$ gives the temperature for each level of the hierarchy, and the Z_l are normalizing constants. In the following, we use this temperature-scaled model to balance the regularization of our inverse problem.

4. Regularization with HVAE Prior

In this section we introduce our Plug-and-Play method using a Hierarchical VAE prior (PnP-HVAE) to solve generic image inverse problems. Building on top of the JPMAP framework [11], we propose a joint model over the image and its latent variable that we optimize in an alternate way. By doing so, we take advantage of the HVAE encoder to avoid backpropagation through the generative network. Although our motivation is similar to JPMAP, PnP-HVAE

¹Note that for the special case $l = 0$, $\mathbf{z}_{<l}$ is empty, meaning that $\Sigma_{\theta,0}(\mathbf{z}_{<0}) = \Sigma_{\theta,0}$ is actually a constant, $q_\phi(\mathbf{z}_0|\mathbf{z}_{<0}, \mathbf{x}) = q_\phi(\mathbf{z}_0|\mathbf{x})$ is only conditioned on \mathbf{x} , etc.

overcomes two of its limitations, that are the lack of control, and the limitation to simple and non-hierarchical VAEs. We show in section 4.1 that the strength of the regularization of the tackled inverse problem can be monitored by tuning the temperature of the prior in the latent space. In section 4.2, we propose an approximation of the joint posterior distribution using the hierarchical VAE encoder. In section 4.3, we present our final algorithm that includes a new greedy scheme to optimize the latent variable of the HVAE.

4.1. Tempered hierarchical joint posterior

The linear image degradation model (1) yields

$$p(\mathbf{y}|\mathbf{x}) \propto e^{-f(\mathbf{x})}, \quad f(\mathbf{x}) = \frac{1}{2\sigma^2} \|\mathbf{A}\mathbf{x} - \mathbf{y}\|^2. \quad (11)$$

Solving the underlying image inverse problem in a bayesian framework requires an a priori distribution $p(\mathbf{x})$ over clean images and studying the posterior distribution of \mathbf{x} knowing its degraded observation \mathbf{y} . In this work, the image prior is given by a hierarchical VAE and we exploit the joint posterior model $p(\mathbf{z}, \mathbf{x}|\mathbf{y})$. From the HVAE latent variable model with reduced temperature $p_{\theta, \tau}(\mathbf{z}_0, \dots, \mathbf{z}_{L-1}, \mathbf{x})$ as defined in (10), we define the associated tempered joint model as:

$$p(\mathbf{z}, \mathbf{x}, \mathbf{y}) := p_{\theta, \tau}(\mathbf{z}_0, \dots, \mathbf{z}_{L-1}, \mathbf{x}) p(\mathbf{y}|\mathbf{x}). \quad (12)$$

Following the JPMAP idea from [11], we aim at finding the couple (\mathbf{x}, \mathbf{z}) that maximizes the joint posterior $p(\mathbf{x}, \mathbf{z}|\mathbf{y})$:

$$\min_{\mathbf{x}, \mathbf{z}} -\log p(\mathbf{x}, \mathbf{z}|\mathbf{y}). \quad (13)$$

Although we are only interested in finding the image \mathbf{x} , the joint Maximum A Posteriori (MAP) criterion (13) makes it possible to derive an optimization scheme that only relies on forward calls of the HVAE. Using Bayes' rule and the definition of the tempered HVAE joint model (12) and (10), the logarithm of the joint posterior rewrites:

$$\begin{aligned} & \log p(\mathbf{x}, \mathbf{z}|\mathbf{y}) + \log p(\mathbf{y}) \\ &= \log p(\mathbf{y}|\mathbf{x}) + \sum_{l=0}^{L-1} \log \frac{p_{\theta}(\mathbf{z}_l|\mathbf{z}_{<l})^{\frac{1}{\tau_l^2}}}{Z_l} + \log p_{\theta}(\mathbf{x}|\mathbf{z}_{<L}). \end{aligned} \quad (14)$$

Since $p(\mathbf{y})$ is constant, finding the joint MAP estimate (13) amounts to minimizing the following criterion:

$$\begin{aligned} J_1(\mathbf{x}, \mathbf{z}) := & -\sum_{l=1}^{L-1} \frac{1}{\tau_l^2} \log p_{\theta}(\mathbf{z}_l|\mathbf{z}_{<l}) \\ & + f(\mathbf{x}) - \log p_{\theta}(\mathbf{x}|\mathbf{z}_{<L}). \end{aligned} \quad (15)$$

Notice that the temperature of the prior over the latent space τ_l controls the weight of the regularization over the latent variable \mathbf{z}_l . Optimizing (15) w.r.t. \mathbf{x} is tractable, whereas the minimization w.r.t. \mathbf{z} requires a backpropagation through the decoder $\log p_{\theta}(\mathbf{x}|\mathbf{z}_{<L})$ that is impractical due to the high dimensionality and the hierarchical structure of the HVAE latent space.

4.2. Encoder approximation of the joint posterior

Using the encoder q_{ϕ} , we can reformulate the joint MAP problem (15) in a form that is more convenient to optimize with respect to \mathbf{z} . Indeed, assuming that the encoder perfectly matches the true posterior, we have that:

$$p_{\theta}(\mathbf{x}|\mathbf{z}) = \frac{q_{\phi}(\mathbf{z}|\mathbf{x})p_{\text{data}}(\mathbf{x})}{p_{\theta}(\mathbf{z})}. \quad (16)$$

This assumption can be met if the variational family $\{q_{\phi}(\cdot|\mathbf{x}); \phi \in \Phi\}$ contains the true posterior $p(\mathbf{z}|\mathbf{x})$ and is trained to optimality, following equation (5). If this assumption appears unrealistic for vanilla (non-hierarchical) VAE [11], our experiments suggest that HVAE is sufficiently expressive to match the posterior to a reasonably good accuracy.

Thus, by introducing the decoder expression (16) in the full model (12), we have:

$$p(\mathbf{z}, \mathbf{x}, \mathbf{y}) = \prod_{l=0}^{L-1} \frac{1}{Z_l} \frac{q_{\phi}(\mathbf{z}_l|\mathbf{z}_{<l}, \mathbf{x})}{p_{\theta}(\mathbf{z}_l|\mathbf{z}_{<l})^{1-\tau_l^{-2}}} p(\mathbf{y}|\mathbf{x}) p_{\text{data}}(\mathbf{x}).$$

Denoting $\lambda_l = \frac{1}{\tau_l^2} - 1$, we reformulate the joint MAP problem (13) as a joint MAP problem over the encoder model:

$$\begin{aligned} \min_{\mathbf{x}, \mathbf{z}} J_2(\mathbf{x}, \mathbf{z}) := & -\sum_{l=0}^{L-1} (\log q_{\phi}(\mathbf{z}_l|\mathbf{x}, \mathbf{z}_{<l}) + \lambda_l \log p_{\theta}(\mathbf{z}_l|\mathbf{z}_{<l})) \\ & + f(\mathbf{x}) - \log p_{\text{data}}(\mathbf{x}). \end{aligned} \quad (17)$$

4.3. Alternate optimization with PnP-HVAE

We introduce an alternate scheme to minimize (13) that sequentially optimizes with respect to \mathbf{x} and to \mathbf{z} . For a linear degradation model and a Gaussian decoder (1), the criterion $J_1(\mathbf{x}, \mathbf{z})$ in (15) is convex in \mathbf{x} and its global minimum is $\mathbf{x} = \left(A^t A + \frac{\sigma^2}{\gamma^2} \text{Id}\right)^{-1} \left(A^t \mathbf{y} + \frac{\sigma^2}{\gamma^2} \mu_{\theta}(\mathbf{z})\right)$. Next we propose to compute an approximate solution of the problem $\min_{\mathbf{z}} J_2(\mathbf{x}, \mathbf{z})$ with the greedy algorithm 1.

Algorithm 1 Hierarchical encoding with latent regularization to minimize (17) w.r.t. \mathbf{z} for a fixed \mathbf{x}

Require: image \mathbf{x} ; HVAE (ϕ, θ) ; temperature τ_l ; $\lambda_l = \frac{1}{\tau_l^2} - 1$

for $0 \leq l < L$ **do**

$S_q \leftarrow \Sigma_{\phi, l}^{-1}(\mathbf{z}_{<l}, \mathbf{x}); m_q \leftarrow \mu_{\phi, l}(\mathbf{z}_{<l}, \mathbf{x})$ ▷ Encoder

$S_p \leftarrow \Sigma_{\theta, l}^{-1}(\mathbf{z}_{<l}); m_p \leftarrow \mu_{\theta, l}(\mathbf{z}_{<l})$ ▷ Prior

$\mathbf{z}_l \leftarrow (S_q + \lambda_l S_p)^{-1} (S_q m_q + \lambda_l S_p m_p)$

end for

return $E_{\tau}(\mathbf{x}) = (\mathbf{z}_0, \mathbf{z}_1, \dots, \mathbf{z}_{L-1})$

In algorithm 1, the latent variables \mathbf{z}_l are determined in a hierarchical fashion starting from the coarsest to the

finest one. As defined in relations (8), the conditionals $q_\phi(z_l|x, z_{<l})$ and $p_\theta(z_l|z_{<l})$ are Gaussian. Therefore, the minimization at each step can be viewed as an interpolation between the mean of the encoder $q_\phi(z_l|x, z_{<l})$ and the prior $p_\theta(z_l|z_{<l})$, given some weights conditioned by the covariance matrices and the temperature τ_l . The solution of each minimization problem in z_l is given by:

$$\hat{z}_l = \left(\Sigma_{\phi,l}^{-1}(\hat{z}_{<l}, \mathbf{x}) + \lambda_l \Sigma_{\theta,l}^{-1}(\hat{z}_{<l}) \right)^{-1} \left(\Sigma_{\phi,l}^{-1}(\hat{z}_{<l}, \mathbf{x}) \mu_{\phi,l}(\hat{z}_{<l}, \mathbf{x}) + \lambda_l \Sigma_{\theta,l}^{-1}(\hat{z}_{<l}) \mu_{\theta,l}(\hat{z}_{<l}) \right) \quad (18)$$

where $\lambda_l = 1/\tau_l^2 - 1$. In the following, we denote as $\hat{z} := E_\tau(\mathbf{x})$ the output of the hierarchical encoding of Algorithm 1. In appendix A.1 we show that this algorithm finds the global optimum of $J_2(\mathbf{x}, \cdot)$ under mild assumptions.

The final PnP-HVAE procedure to solve an inverse problem with the HVAE prior is presented in Algorithm 2.

Algorithm 2 PnP-HVAE - Restoration by solving (15)

```

 $k \leftarrow 0; res \leftarrow +\infty$ ; initialize  $\mathbf{x}^{(0)}$ 
while  $res > tol$  do
    %  $\min_z J_2(\mathbf{x}^{(k)}, z) \triangleright$  Optimize (17) w.r.t.  $z$  using Alg. 1
     $\mathbf{z}^{(k+1)} = E_\tau(\mathbf{x}^{(k)})$ 
    %  $\min_x J_1(\mathbf{x}, \mathbf{z}^{(k+1)}) \triangleright$  Optimize (15) w.r.t.  $\mathbf{x}$ 
     $\mathbf{x}^{(k+1)} = \left( A^t A + \frac{\sigma^2}{\gamma^2} \text{Id} \right)^{-1} \left( A^t \mathbf{y} + \frac{\sigma^2}{\gamma^2} \mu_\theta(\mathbf{z}^{(k+1)}) \right)$ 
     $res \leftarrow \|\mathbf{x}^{(k+1)} - \mathbf{x}^{(k)}\|$ ;  $k \leftarrow k + 1$ 
end while
return  $\mathbf{x}^{(k)}$ 

```

5. Convergence analysis

We now analyse the convergence of Algorithm 2. Following the work of [3], the alternate optimization scheme converges if $q_\phi(z|x) = p_\theta(z|x)$ and the greedy optimization scheme in Algorithm 1 actually solves $\min_z J_2(\mathbf{x}, z)$. In practice, it is difficult to verify if these hypotheses hold. We propose to theoretically study algorithm 2, and next verify empirically that the assumptions are met.

In section 5.1, we reformulate Algorithm 2 as a Plug-and-Play algorithm, where the HVAE reconstruction takes the role of the denoiser. Then we study in section 5.2 the fixed-point convergence of the algorithm. Finally, section 5.3 contains numerical experiments with the patch HVAE architecture proposed in section 6.2. We empirically show that the patch architecture satisfies the aforementioned technical assumptions and then illustrate the numerical convergence and the stability of our alternate algorithm.

5.1. Plug-and-Play HVAE

In this section we make the assumption that the HVAE decoder is Gaussian with a constant variance on its diag-

onal (9). We rely on the proximal operator of a convex function f that is defined as $\text{prox}_f(\mathbf{x}) = \arg \min_{\mathbf{u}} f(\mathbf{u}) + \frac{1}{2} \|\mathbf{x} - \mathbf{u}\|^2$.

Proposition 1 Assume the decoder is defined as in (9). Denote $HVAE(\mathbf{x}, \tau) := \mu_\theta(E_\tau(\mathbf{x}))$. Then the alternate scheme described in Algorithm 2 writes

$$\mathbf{x}_{k+1} = \text{prox}_{\gamma^2 f}(HVAE(\mathbf{x}_k, \tau)). \quad (19)$$

From relation (19), algorithm 2 is a Plug-and-Play Half-Quadratic Splitting method [45] where the role of the denoiser is played by the reconstruction $HVAE(\mathbf{x}_k, \tau)$. We now derive from relation (19) sufficient conditions to establish the convergence of the iterations.

5.2. Fixed-point convergence

Let us denote T the operator corresponding to one iteration of (19): $T(\mathbf{x}) = \text{prox}_{\gamma^2 f}(HVAE(\mathbf{x}, \tau))$. The Lipschitz constant of T can then be expressed as a function of f and the HVAE reconstruction operator $HVAE(\mathbf{x}_k, \tau)$.

Proposition 2 (Proof in supplementary) Assume that the decoder has a constant variance $\Sigma_\theta^{-1}(\mathbf{z}) = \frac{1}{\gamma^2} \text{Id}$ for all \mathbf{z} ; and the autoencoder with latent regularization is L_τ -Lipschitz, i.e. $\forall \mathbf{u}, \mathbf{v} \in \mathbb{R}^n$: $\|HVAE(\mathbf{u}, \tau) - HVAE(\mathbf{v}, \tau)\| \leq L_\tau \|\mathbf{u} - \mathbf{v}\|$. Then, denoting as λ_{\min} the smallest eigenvalue of $A^t A$, we have

$$\|T(\mathbf{u}) - T(\mathbf{v})\| \leq \frac{\sigma^2}{\gamma^2 \lambda_{\min} + \sigma^2} L_\tau \|\mathbf{u} - \mathbf{v}\|. \quad (20)$$

Corollary 1 If $HVAE(\mathbf{x}_k, \tau)$ is $L_\tau < 1$ -Lipschitz, then iterations (19) converge.

Proof. If $L_\tau < 1$, then $HVAE(\mathbf{x}_k, \tau)$ is a contraction. Hence T is also a contraction form proposition 2 and consequently, Banach theorem ensures the convergence of the iteration $\mathbf{x}_{k+1} = T(\mathbf{x}_k)$ to a fixed point of T . \square

Proposition 3 (Proof in supplementary) \mathbf{x}^* is a fixed point of T if and only if:

$$\nabla f(\mathbf{x}^*) = \frac{1}{\gamma^2} (HVAE(\mathbf{x}^*, \tau) - \mathbf{x}^*) \quad (21)$$

Proposition 3 characterizes the solution of the latent-regularization scheme, in the case where the HVAE reconstruction is a contraction. Under mild assumptions, the fixed point condition can be stated as a critical point condition

$$\nabla f(\mathbf{x}^*) + \nabla g(\mathbf{x}^*) = 0,$$

of the objective function $f(\mathbf{x}) + g(\mathbf{x}) = -\log p(\mathbf{y}|\mathbf{x}) - \log p_{\theta, \tau}(\mathbf{x})$, where the tempered prior is the marginal $p_{\theta, \tau}(\mathbf{x}) := \int p_{\theta, \tau}(\mathbf{x}, \mathbf{z}) d\mathbf{z}$ of the joint tempered prior defined in (10). This result, detailed in the supplementary, follows from an interpretation of $HVAE(\mathbf{x}, \tau)$ as an MMSE denoiser. As a consequence Tweedie's formula provides the link between the right-hand side of equation (21) and ∇g .

5.3. Numerical convergence with PatchVDVAE

We illustrate the numerical convergence of Algorithm 2. We first analyse the Lipschitz constant of the HVAE reconstruction with the PatchVDVAE architecture proposed in section 6.2. Then we study the empirical convergence of the algorithm and show that it outperforms the baseline optimisation of the joint MAP (15) with the Adam optimizer.

Lipschitz constant of the HVAE reconstruction. Corollary 1 establishes the fixed point convergence of our proposed optimization algorithm under the hypothesis that the reconstruction with latent regularization is a contraction, *i.e.* $L_\tau < 1$. We now show thanks to an empirical estimation of the Lipschitz constant L_τ that our PatchVDVAE network empirically satisfies such a property when applied to noisy images. We present in figure 1 the histograms of the ratios $r = \|\text{HVAE}(\mathbf{u}, \tau) - \text{HVAE}(\mathbf{v}, \tau)\| / \|\mathbf{u} - \mathbf{v}\|$, where \mathbf{u} and \mathbf{v} are natural images extracted from the BSD dataset and corrupted with white Gaussian noise. These ratios give a lower bound for the true Lipschitz constant L_τ . Although it is possible to set different temperature τ_l at each level, we fixed a constant temperature amongst all levels to limit the number of hyperparameters. We realized tests for 3 temperatures $\tau \in \{0.6, 0.8, 0.99\}$, and 3 noise levels $\sigma \in \{0, 25, 50\}$. On clean images ($\sigma = 0$), the distribution of ratios is close to 1. This suggests that the HVAE is well trained and accurately models clean images. In some rare case, a ratio $r \geq 1$ is observed for clean images. This indicates that the reconstruction is not a contraction everywhere, in particular on the manifold of clean images.

On noisy images $\sigma > 0$, the reconstruction behaves as a contraction, as the ratio $r < 1$ is always observed. Moreover, reducing the temperature of the latent regularization τ increases the strength of the contraction. This suggests that with the trained PatchVDVAE architecture, the hypothesis $L_\tau < 1$ in Corollary 1 holds for noisy images.

Convergence of Algorithm 2 We now illustrate the effectiveness of PnP-HVAE through comparisons with the optimization of the objective $J_1(\mathbf{x}_k, \mathbf{z}_k)$ in (15) using the Adam algorithm [23] for two learning rates $lr \in \{0.01, 0.001\}$. The left plot in figure 2 shows that Adam is able to estimate a better minimum of J_1 . However, our alternate algorithm requires a smaller number of iterations to converge.

On the other hand, as illustrated by the right plot in figure 2, the use of Adam involves numerical instabilities. Oscillations of the ratio $L_k := \frac{\|\mathbf{T}(\mathbf{x}_{k+1}) - \mathbf{T}(\mathbf{x}_k)\|}{\|\mathbf{x}_{k+1} - \mathbf{x}_k\|}$ are even increased with larger learning rates, whereas our method provides a stable sequence of iterates.

More important, we finally exhibit the better quality of the restorations obtained with our alternate algorithm on inpainting, deblurring and super-resolution of face images. In these experiments, we used the hierarchical VDVAE model [6] trained on the FFHQ dataset [20]. Figure 3 (see 2nd and 4th columns) and table 1 (PSNR, SSIM and LPIPS

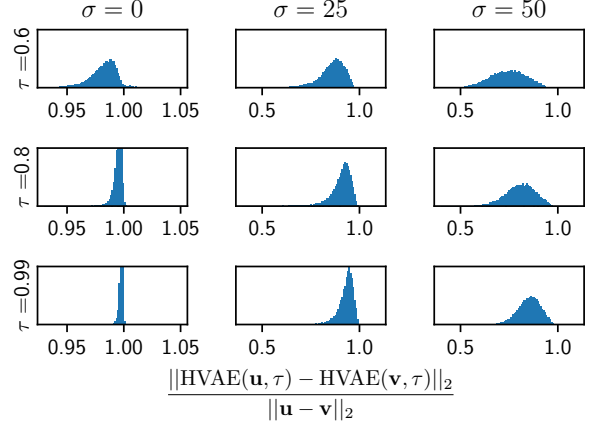


Figure 1: Numerical estimation of the Lipschitz constant of PatchVDVAE reconstruction with different temperatures τ . We present the histogram of ratio values $\frac{\|\text{HVAE}(\mathbf{u}, \tau) - \text{HVAE}(\mathbf{v}, \tau)\|_2}{\|\mathbf{u} - \mathbf{v}\|_2}$, where \mathbf{u} and \mathbf{v} are natural images corrupted with white Gaussian noise of different standard deviations σ . For noisy images ($\sigma > 0$), the observed Lipschitz constant is always less than 1.

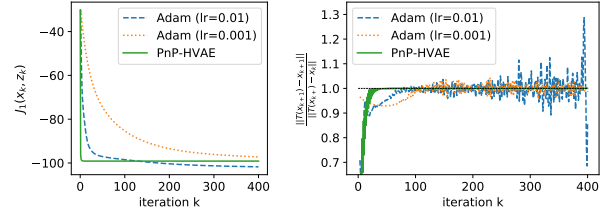


Figure 2: Comparison of the convergence of PnP-HVAE algorithm 2 with respect to the baseline Adam optimizer, on a deblurring problem. Left (Convergence of the function value): PnP-HVAE converges faster to a minimum of the joint posterior $J_1(\mathbf{x}_k, \mathbf{z}_k)$ in (15). Right (Convergence of iterates \mathbf{x}_k): PnP-HVAE is more stable than Adam.

scores) illustrate that the quality of the images restored with our alternate optimization algorithm is higher than the ones obtained with Adam. This suggests that for image restoration purposes, our optimization method is able to find a more relevant local minimum of J_1 than Adam.

6. Image restoration results

We present in section 6.1 an application of PnP-HVAE on face images, using a pretrained state-of-the-art hierarchical VAE. Next, we study the application of our framework to natural images. To that end, we introduce in section 6.2 a patch hierarchical VAE architecture, that is able to model natural images of different resolutions. In section 6.3, we provide deblurring, super-resolution and inpainting experiments to demonstrate the relevance of the proposed method.

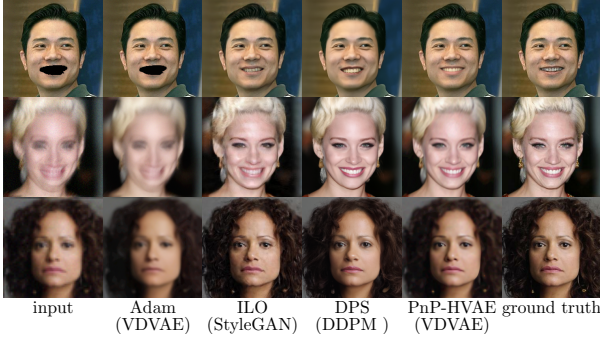


Figure 3: Visual comparison of image restoration methods based on deep generative models. We studied 3 tasks on face images: inpainting (top), deblurring (middle), super-resolution (bottom). Contrary to the optimization of the objective (15) with Adam, our alternate algorithm generates realistic results, on par with ILO [8], while remaining consistent with the observation.

		PSNR \uparrow	SSIM \uparrow	LPIPS \downarrow	time (s)
SR $\times 4$ $\sigma = 3$	Adam	28.56	0.75	0.38	<u>26</u>
	ILO	<u>28.80</u>	<u>0.78</u>	0.17	34
	PnP-HVAE	29.32	0.82	0.28	15
	DPS	27.53	0.76	<u>0.21</u>	153
Deblurring (motion) $\sigma = 8$	Adam	26.69	0.75	0.27	<u>12</u>
	ILO	<u>29.01</u>	<u>0.80</u>	<u>0.20</u>	34
	PnP-HVAE	30.40	0.84	0.16	10
	DPS	28.70	<u>0.80</u>	0.23	142
Deblurring (Gaussian) $\sigma = 8$	Adam	<u>30.17</u>	<u>0.83</u>	<u>0.21</u>	<u>12</u>
	ILO	29.12	0.79	0.17	34
	PnP-HVAE	30.81	0.86	0.24	10
	DPS	29.14	0.81	0.24	142

Table 1: Quantitative evaluation on face restoration. Best results in **bold**, second best underlined.

6.1. Face Image restoration (FFHQ)

We first demonstrate the effectiveness of PnP-HVAE on highly structured data, by performing face image restoration. Latent variable generative models can accurately model structured images such as face images [20, 53, 6, 24], and then be used to produce high quality restoration of such data. In our experiments, we use the VDVAE model of [6], pre-trained on the FFHQ dataset [20], as our hierarchical VAE prior. VDVAE has $L = 66$ latent variable groups in its hierarchy and generates images at resolution 256×256 .

We compare PnP-HVAE with two restoration methods based on different class of generative models, namely the intermediate layer optimization algorithm (ILO) [8] and the diffusion posterior sampling method (DPS) [7]. ILO is a GAN inversion method which optimizes the image latent code along with the intermediate layer representation of a StyleGAN2 generative network [21] to generate an image consistent with a degraded observation. DPS use denoising

diffusion probabilistic model [52, 16] as a prior, and produce a sample from the posterior by conditioning each iteration of the sampling process on y . We use the official implementation of ILO, along with a StyleGAN2 model that was trained for 550k iterations on images of resolution 256×256 from FFHQ [44]. For DPS, we use the official implementation as well. As VDVAE and StyleGAN models are not trained on the same train-test split of FFHQ, we chose to evaluate the methods on a subset of 100 images from the CelebA dataset [29]. For super-resolution, the degradation model corresponds to the application of a Gaussian low-pass filter followed by a $\times 4$ sub-sampling, and the addition of a Gaussian white noise with $\sigma = 3$. For the deblurring, we considered motion blur and Gaussian kernels, both with a noise level $\sigma = 8$.

We provide quantitative comparisons in table 1, along with a visual comparison of the results in figure 3. PnP-HVAE has the best PSNR and SSIM results for all the considered restoration tasks, while ILO provides better results for the perceptual distance. By jointly optimizing the image and its latent variable, PnP-HVAE provides results that are both realistic and consistent with the degraded observation. On the other hand, ILO only optimizes on an extended latent space. This method generates sharp and realistic images with better LPIPS scores, but the results lack of consistency with respect to the observation, which explains the overall lower PSNR performance. DPS produces highly realistic samples, however DPS is limited by its long inference time, as it requires one network function evaluation and one backpropagation operation through the network at each of the 1000 sampling steps required to generate one image.

6.2. PatchVDVAE: a HVAE for natural images

Available generative models in the literature operate on images of fixed resolutions and are either restrained to datasets of limited diversity, or even to registered face images [24, 6, 53, 20], or requiring additional class information [5, 9, 52, 31]. Fitting an unconditional model on natural images appears to be a more difficult task, as their resolution can change, and their content is highly diverse. The complexity of the problem can be reduced by learning a prior model on patches of reduced dimension. For image restoration problems, the patch model can be reused on images of higher dimensions [57, 39, 2]. When the model is a full CNN, the prior on the set of the patches can be computed efficiently by applying the network on the full image [39].

We thus introduce patchVDVAE, a fully convolutional hierarchical VAE. Contrary to existing HVAE models whose resolution is constrained by the constant tensor at the input of the top-down block, patchVDVAE can generate images of different resolutions by controlling the dimension of the input latent. This amounts to defining a prior on patches

whose dimension corresponds to the receptive field of the VAE. A similar model is used for image denoising in [38].

For PatchVDVAE architecture, we use the same bottom-up and top-down blocks as VDVAE [6], and replace the constant trainable input in the first top-down block by a latent variable, to make the model fully convolutional (details on the architecture are given in the supplementary). The training dataset is composed of 128×128 patches extracted from a combination of DIV2K [1] and Flickr2K [28] datasets. We perform data augmentation by extracting patches at 3 resolutions: HR-images and $\times 2$ and $\times 4$ downsampled images. The model is trained for 7.10^5 iterations with a batch size of 64. Following the recommendation of [15], we use Adamax optimizer with an exponential moving average and gradient smoothing of the variance. We set the decoder model to be a Gaussian with diagonal covariance, as in [31]. PatchVDVAE is fully convolutional and can generate images of dimension that are multiples of 64 as illustrated by figure 4.



Figure 4: Left: 64×64 patches samples from our patchVDVAE model trained on patches from natural images. Right: PatchVDVAE is fully convolutional and it can generate images of higher resolution (here: 128×128).

6.3. Natural images restoration

We evaluate PnP-HVAE on natural image restoration. For each task, we report the average value of the PSNR, the SSIM, and the LPIPS metrics on 20 images from the test set of the BSD dataset [32].

Image deblurring. In the experiments, we consider 2 Gaussian kernels and 2 motion blur kernels from [27], with 3 different noise levels $\sigma \in \{2.55, 7.65, 12.75\}$. As a baseline we consider EPLL [57], which learns a prior on image patches with a Gaussian mixture model. We also compare PnP-HVAE with PnP-MMO and GS-PnP, 2 competing convergent Plug-and-Play methods based on CNN denoisers. PnP-MMO [37] restricts the denoiser to be contraction in order to guarantee the convergence of the PnP forward-backward algorithm. GS-PnP [19] considers a gradient step denoiser and reaches state-of-the-art performances of non converging methods [55]. We set the temperature τ in our method as 0.95, 0.8 and 0.6 for noise levels 2.55, 7.65 and 12.75 respectively, and we let it run for a maximum of 50 iterations. For the three compared methods we use the official implementations and pre-trained models provided by the respective authors. Details on the choice of hyperparameters

σ	Method	PSNR \uparrow	SSIM \uparrow	LPIPS \downarrow
2.55	PnP-HVAE	27.75	0.79	0.31
	GS-PnP [19]	29.59	0.84	0.22
	EPLL [57]	26.49	0.71	0.36
	PnP-MMO [37]	<u>29.50</u>	<u>0.83</u>	<u>0.20</u>
7.65	PnP-HVAE	<u>26.36</u>	<u>0.72</u>	<u>0.40</u>
	GS-PnP [19]	27.33	0.77	0.31
	EPLL [57]	24.04	0.66	0.45
	PnP-MMO [37]	25.34	0.69	0.34
12.75	PnP-HVAE	<u>25.12</u>	0.73	<u>0.47</u>
	GS-PnP [19]	26.32	0.73	0.37
	EPLL [57]	23.28	0.61	0.51
	PnP-MMO [37]	22.42	0.53	0.54

Blur and motion kernels

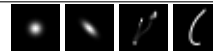
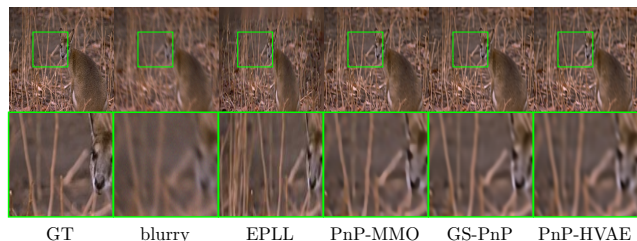
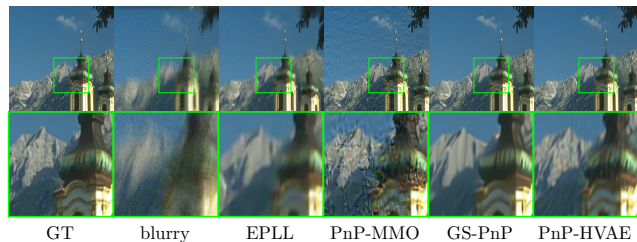


Table 2: Comparison of PnP-HVAE and other restoration methods on deblurring. Results are averaged on 4 kernels.



(a) Gaussian blur, $\sigma = 2.55$



(b) Motion blur, $\sigma = 7.65$

Figure 5: Natural image deblurring

for the concurrent methods are provided in the supplementary material. Figure 5 illustrates that our method provides correct deblurring results. According to table 2, the performance of PnP-HVAE is between those of EPLL and GS-PnP and it outperforms PnP-MMO for large noise levels.

Image inpainting. Next we consider the task of noisy image inpainting. We compose a test-set of 10 images from the validation set of BSD [32] and we create masks by occluding diverse objects of small size in the images. A Gaussian white noise with $\sigma = 3$ is added to the images. As a comparison, we still consider GS-PnP and EPLL. For PnP-HVAE, the temperature is set to $\tau = 0.6$, and the algorithm is run for a maximum of 200 iterations, unless the residual $\|x_{k+1} - x_k\|$ is on a plateau. We provide on Table 3 the distortion metrics with the ground truth, as well as a visual comparison on figure 6. With its hierarchical structure,

	PSNR \uparrow	SSIM \uparrow	LPIPS \downarrow
PnP-HVAE	29.54	0.93	0.06
GS-PnP	28.52	0.93	0.09
EPLL	<u>29.16</u>	0.93	0.06

Table 3: Quantitative evaluation for inpainting on BSD.

PnP-HVAE outperforms the compared methods.

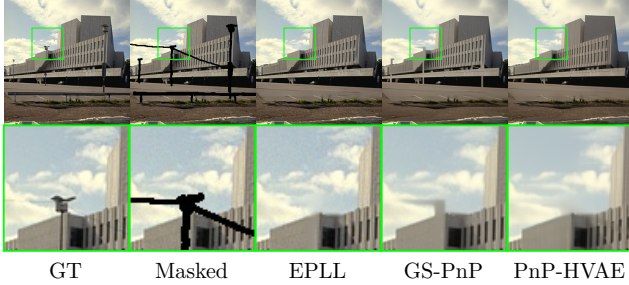


Figure 6: Natural image inpainting

Effect of the temperature. PnP-HVAE gives control on the temperature of the prior over the latent space. In figure 7, we illustrate that reducing the temperature increases the strength of the regularization prior. In this example the tuning $\tau = 0.7$ produces the best performance.

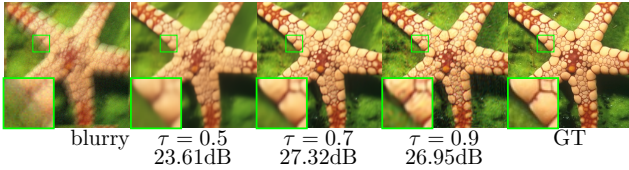


Figure 7: Effect of the temperature in PnP-VAE on a deblurring problem, with $\sigma = 7.65$.

Effect of the number of latent groups We study the effect of the number of latent groups L on the hierarchical model on the restoration performance. It has been observed that HVAEs outperform non-hierarchical VAEs in terms of likelihood score [49], and that increasing the number of latent groups in the hierarchy improves the modelling performance of HVAE for a fixed number of parameters [6]. Therefore we can expect that the gain in modelling performance due to a higher L will translate into a gain in restoration performance using our method. We train different patchVDVAE models, with different number of latent groups L . In order to keep the number of trainable parameters constant, we replace stochastic top-down blocks with deterministic blocks in our network with the higher L value ($L = 36$). We evaluate the different models on image deblurring, using the same experimental settings as the one described in subsection 6.3. The results in table 4 show that increasing the number of stochastic groups (L) has a posi-

Table 4: Effect of the number L of latent groups on the restoration performance, measured in PSNR (dB), for image deblurring. We observed similar trends for the LPIPS and SSIM metrics.

	$L = 6$	$L = 12$	$L = 18$	$L = 36$
$\sigma = 2.55$	27.25	27.87	<u>27.82</u>	27.71
$\sigma = 7.65$	26.10	26.41	26.74	<u>26.51</u>
$\sigma = 12.75$	24.78	25.16	25.57	<u>25.27</u>
ELBO \uparrow (val)	-1.24	-1.14	-1.10	-1.10

tive effect on the validation ELBO, up to $L = 18$, and that a better ELBO correlates with a better restoration performance.

7. Conclusion

We proposed PnP-HVAE, a method using hierarchical variational autoencoders as a prior to solve image inverse problems. Motivated by an alternate optimization scheme, PnP-HVAE exploits the encoder of the HVAE to avoid backpropagating through the generative network. We derived sufficient conditions on the HVAE model to guarantee the convergence of the algorithm. We have verified empirically that PnP-HVAE satisfies those conditions. By jointly optimizing over the image and the latent space, PnP-HVAE produces realistic results that are more consistent with the observation than GAN inversion on a specialized dataset. PnP-HVAE can also restore natural images of any size using our PatchVDVAE model trained on natural images patches.

Acknowledgements

This study has been carried out with financial support from the French Research Agency through the Post-ProdLEAP project (ANR-19-CE23-0027-01). Experiments presented in this paper were carried out using the PlaFRIM experimental testbed, supported by Inria, CNRS (LABRI and IMB), Université de Bordeaux, Bordeaux INP and Conseil Régional d’Aquitaine (see <https://www.plafrim.fr>)

References

- [1] Eirikur Agustsson and Radu Timofte. Ntire 2017 challenge on single image super-resolution: Dataset and study. In *Proceedings of the IEEE conference on computer vision and pattern recognition workshops*, pages 126–135, 2017. [8](#)
- [2] Fabian Altekürer, Alexander Denker, Paul Hagemann, Johannes Hertrich, Peter Maass, and Gabriele Steidl. Patchnr: learning from very few images by patch normalizing flow regularization. *Inverse Problems*, 39(6):064006, 2023. [7](#)
- [3] Hédý Attouch, Jérôme Bolte, Patrick Redont, and Antoine Soubeyran. Proximal alternating minimization and projection methods for nonconvex problems: An approach based on the kurdyka-łojasiewicz inequality. *Mathematics of operations research*, 35(2):438–457, 2010. [5](#)
- [4] Ashish Bora, Ajil Jalal, Eric Price, and Alexandros G Dimakis. Compressed sensing using generative models. In *International Conference on Machine Learning*, pages 537–546. PMLR, 2017. [1](#), [2](#)
- [5] Andrew Brock, Jeff Donahue, and Karen Simonyan. Large scale gan training for high fidelity natural image synthesis. In *International Conference on Learning Representations*, 2018. [7](#)
- [6] Rewon Child. Very deep vaes generalize autoregressive models and can outperform them on images. In *International Conference on Learning Representations*, 2020. [1](#), [2](#), [3](#), [6](#), [7](#), [8](#), [9](#), [19](#)
- [7] Hyungjin Chung, Jeongsol Kim, Michael Thompson McCann, Marc Louis Klasky, and Jong Chul Ye. Diffusion posterior sampling for general noisy inverse problems. In *The Eleventh International Conference on Learning Representations*, 2022. [3](#), [7](#), [19](#)
- [8] Giannis Daras, Joseph Dean, Ajil Jalal, and Alex Dimakis. Intermediate layer optimization for inverse problems using deep generative models. In *International Conference on Machine Learning*, pages 2421–2432. PMLR, 2021. [2](#), [7](#)
- [9] Prafulla Dhariwal and Alexander Nichol. Diffusion models beat gans on image synthesis. *Advances in Neural Information Processing Systems*, 34:8780–8794, 2021. [7](#)
- [10] Laurent Dinh, Jascha Sohl-Dickstein, and Samy Bengio. Density estimation using real nvp. In *International Conference on Learning Representations*, 2016. [2](#)
- [11] Mario González, Andrés Almansa, and Pauline Tan. Solving inverse problems by joint posterior maximization with autoencoding prior. *SIAM Journal on Imaging Sciences*, 15(2):822–859, 2022. [2](#), [3](#), [4](#)
- [12] Ian Goodfellow, Jean Pouget-Abadie, Mehdi Mirza, Bing Xu, David Warde-Farley, Sherjil Ozair, Aaron Courville, and Yoshua Bengio. Generative adversarial networks. *Communications of the ACM*, 63(11):139–144, 2020. [2](#)
- [13] Paul Hand, Oscar Leong, and Vlad Voroninski. Phase retrieval under a generative prior. *Advances in Neural Information Processing Systems*, 31, 2018. [2](#)
- [14] Jakob D Havtorn, Jes Frellsen, Søren Hauberg, and Lars Maaløe. Hierarchical vaes know what they don’t know. In *International Conference on Machine Learning*, pages 4117–4128. PMLR, 2021. [2](#), [3](#)
- [15] Louay Hazami, Rayhane Mama, and Ragavan Thuraiatnam. Efficient-vdvae: Less is more. *arXiv preprint arXiv:2203.13751*, 2022. [1](#), [8](#)
- [16] Jonathan Ho, Ajay Jain, and Pieter Abbeel. Denoising diffusion probabilistic models. *Advances in Neural Information Processing Systems*, 33:6840–6851, 2020. [2](#), [3](#), [7](#)
- [17] Matthew Holden, Marcelo Pereyra, and Konstantinos C Zygalakis. Bayesian imaging with data-driven priors encoded by neural networks. *SIAM Journal on Imaging Sciences*, 15(2):892–924, 2022. [2](#)
- [18] Wen Huang, Paul Hand, Reinhard Heckel, and Vladislav Voroninski. A provably convergent scheme for compressive sensing under random generative priors. *Journal of Fourier Analysis and Applications*, 27:1–34, 2021. [2](#)
- [19] Samuel Hurault, Arthur Leclaire, and Nicolas Papadakis. Gradient step denoiser for convergent plug-and-play. In *International Conference on Learning Representations*, 2022. [2](#), [8](#)
- [20] Tero Karras, Samuli Laine, and Timo Aila. A style-based generator architecture for generative adversarial networks. In *Proceedings of the IEEE/CVF conference on computer vision and pattern recognition*, pages 4401–4410, 2019. [2](#), [6](#), [7](#)
- [21] Tero Karras, Samuli Laine, Miika Aittala, Janne Hellsten, Jaakko Lehtinen, and Timo Aila. Analyzing and improving the image quality of stylegan. In *Proceedings of the IEEE/CVF conference on computer vision and pattern recognition*, pages 8110–8119, 2020. [7](#)
- [22] Bahjat Kavar, Michael Elad, Stefano Ermon, and Jiaming Song. Denoising Diffusion Restoration Models. In *ICLR Workshop on Deep Generative Models for Highly Structured Data*, volume 2020-Decem, jan 2022. [3](#)
- [23] Diederik Kingma and Jimmy Ba. Adam: A method for stochastic optimization. In *International Conference on Learning Representations (ICLR)*, San Diego, CA, USA, 2015. [6](#)
- [24] Durk P Kingma and Prafulla Dhariwal. Glow: Generative flow with invertible 1x1 convolutions. *Advances in neural information processing systems*, 31, 2018. [7](#)
- [25] Diederik P. Kingma and Max Welling. Auto-Encoding Variational Bayes. In *2nd International Conference on Learning Representations, ICLR 2014, Banff, AB, Canada, April 14-16, 2014, Conference Track Proceedings*, 2014. [2](#), [3](#)
- [26] Fabian Latorre, Volkan Cevher, et al. Fast and provable admm for learning with generative priors. *Advances in Neural Information Processing Systems*, 32, 2019. [2](#)
- [27] Anat Levin, Yair Weiss, Fredo Durand, and William T Freeman. Understanding and evaluating blind deconvolution algorithms. In *2009 IEEE conference on computer vision and pattern recognition*, pages 1964–1971. IEEE, 2009. [8](#), [23](#)
- [28] Bee Lim, Sanghyun Son, Heewon Kim, Seungjun Nah, and Kyoung Mu Lee. Enhanced deep residual networks for single image super-resolution. In *The IEEE Conference on Computer Vision and Pattern Recognition (CVPR) Workshops*, July 2017. [8](#)
- [29] Ziwei Liu, Ping Luo, Xiaogang Wang, and Xiaoou Tang. Large-scale celebfaces attributes (celeba) dataset. *Retrieved August*, 15(2018):11, 2018. [7](#)

- [30] Andreas Lugmayr, Martin Danelljan, Andres Romero, Fisher Yu, Radu Timofte, and Luc Van Gool. RePaint: Inpainting using Denoising Diffusion Probabilistic Models. In *(CVPR) Conference on Computer Vision and Pattern Recognition*, pages 11451–11461. IEEE, jun 2022. 3
- [31] Eric Luhman and Troy Luhman. Optimizing hierarchical image vaes for sample quality. *arXiv preprint arXiv:2210.10205*, 2022. 1, 7, 8
- [32] D. Martin, C. Fowlkes, D. Tal, and J. Malik. A database of human segmented natural images and its application to evaluating segmentation algorithms and measuring ecological statistics. In *Proc. 8th Int'l Conf. Computer Vision*, volume 2, pages 416–423, July 2001. 8
- [33] Xiangming Meng and Yoshiyuki Kabashima. Diffusion Model Based Posterior Sampling for Noisy Linear Inverse Problems. nov 2022. 3
- [34] Sachit Menon, Alexandru Damian, Shijia Hu, Nikhil Ravi, and Cynthia Rudin. Pulse: Self-supervised photo upsampling via latent space exploration of generative models. In *Proceedings of the IEEE/CVF conference on computer vision and pattern recognition*, pages 2437–2445, 2020. 1, 2
- [35] Thomas Oberlin and Mathieu Verm. Regularization via deep generative models: an analysis point of view. In *2021 IEEE International Conference on Image Processing (ICIP)*, pages 404–408, 2021. 2
- [36] Xingang Pan, Xiaohang Zhan, Bo Dai, Dahua Lin, Chen Change Loy, and Ping Luo. Exploiting deep generative prior for versatile image restoration and manipulation. *IEEE Transactions on Pattern Analysis and Machine Intelligence*, 44(11):7474–7489, 2021. 2
- [37] Jean-Christophe Pesquet, Audrey Repetti, Matthieu Terris, and Yves Wiaux. Learning maximally monotone operators for image recovery. *SIAM Journal on Imaging Sciences*, 14(3):1206–1237, 2021. 2, 8
- [38] Mangal Prakash, Mauricio Delbracio, Peyman Milanfar, and Florian Jug. Interpretable unsupervised diversity denoising and artefact removal. In *International Conference on Learning Representations*, 2021. 8
- [39] Jean Prost, Antoine Houdard, Andrés Almansa, and Nicolas Papadakis. Learning local regularization for variational image restoration. In *Scale Space and Variational Methods in Computer Vision: 8th International Conference, SSVM 2021, Virtual Event, May 16–20, 2021, Proceedings*, pages 358–370. Springer, 2021. 7
- [40] Ankit Raj, Yuqi Li, and Yoram Bresler. Gan-based projector for faster recovery with convergence guarantees in linear inverse problems. In *Proceedings of the IEEE/CVF International Conference on Computer Vision*, pages 5602–5611, 2019. 2
- [41] Danilo Rezende and Shakir Mohamed. Variational inference with normalizing flows. In *International conference on machine learning*, pages 1530–1538. PMLR, 2015. 2
- [42] Danilo Jimenez Rezende, Shakir Mohamed, and Daan Wierstra. Stochastic backpropagation and approximate inference in deep generative models. In *International conference on machine learning*, pages 1278–1286. PMLR, 2014. 3
- [43] Yaniv Romano, Michael Elad, and Peyman Milanfar. The little engine that could: Regularization by denoising (red). *SIAM J. on Im. Sc.*, 10(4):1804–1844, 2017. 2
- [44] Kim Seonghyeon (rosinality). stylegan2-pytorch. <https://github.com/rosinality/stylegan2-pytorch>, 2020. 7
- [45] Ernest Ryu, Jialin Liu, Sicheng Wang, Xiaohan Chen, Zhangyang Wang, and Wotao Yin. Plug-and-play methods provably converge with properly trained denoisers. In *International Conference on Machine Learning*, pages 5546–5557. PMLR, 2019. 2, 5
- [46] Chitwan Saharia, William Chan, Huiwen Chang, Chris Lee, Jonathan Ho, Tim Salimans, David Fleet, and Mohammad Norouzi. Palette: Image-to-Image Diffusion Models. In *(SIGGRAPH) Special Interest Group on Computer Graphics and Interactive Techniques Conference Proceedings*, number 1, pages 1–10, New York, NY, USA, aug 2022. ACM. 3
- [47] Chitwan Saharia, Jonathan Ho, William Chan, Tim Salimans, David J. Fleet, and Mohammad Norouzi. Image Super-Resolution via Iterative Refinement. *IEEE Transactions on Pattern Analysis and Machine Intelligence*, pages 1–14, apr 2021. 1, 3
- [48] Viraj Shah and Chinmay Hegde. Solving linear inverse problems using gan priors: An algorithm with provable guarantees. In *2018 IEEE international conference on acoustics, speech and signal processing (ICASSP)*, pages 4609–4613. IEEE, 2018. 2
- [49] Casper Kaae Sønderby, Tapani Raiko, Lars Maaløe, Søren Kaae Sønderby, and Ole Winther. Ladder variational autoencoders. *Advances in neural information processing systems*, 29, 2016. 9
- [50] Jiaming Song, Arash Vahdat, Morteza Mardani, and Jan Kautz. Pseudoinverse-Guided Diffusion Models for Inverse Problems. In *(ICLR) International Conference on Learning Representations*, 2023. 3
- [51] Yang Song, Liye Shen, Lei Xing, and Stefano Ermon. Solving inverse problems in medical imaging with score-based generative models. In *International Conference on Learning Representations*, 2021. 2
- [52] Yang Song, Jascha Sohl-Dickstein, Diederik P Kingma, Abhishek Kumar, Stefano Ermon, and Ben Poole. Score-based generative modeling through stochastic differential equations. In *International Conference on Learning Representations*, 2020. 2, 7
- [53] Arash Vahdat and Jan Kautz. Nvae: A deep hierarchical variational autoencoder. *Advances in neural information processing systems*, 33:19667–19679, 2020. 1, 3, 7
- [54] Singanallur V Venkatakrishnan, Charles A Bouman, and Brendt Wohlberg. Plug-and-play priors for model based reconstruction. In *2013 IEEE Global Conference on Signal and Information Processing*, pages 945–948. IEEE, 2013. 2
- [55] Kai Zhang, Yawei Li, Wangmeng Zuo, Lei Zhang, Luc Van Gool, and Radu Timofte. Plug-and-play image restoration with deep denoiser prior. *IEEE Transactions on Pattern Analysis and Machine Intelligence*, 44(10):6360–6376, 2021. 2, 8

- [56] Shengjia Zhao, Jiaming Song, and Stefano Ermon. Learning hierarchical features from deep generative models. In *International Conference on Machine Learning*, pages 4091–4099. PMLR, 2017. [3](#)
- [57] Daniel Zoran and Yair Weiss. From learning models of natural image patches to whole image restoration. In *2011 international conference on computer vision*, pages 479–486. IEEE, 2011. [7](#), [8](#)

Summary

This supplementary material contains:

- proofs of the theoretical results of the main paper in section **A**
- additional implementation details in section **B**
- a discussion on the contractivity of the autoencoder and its fixed points in section **C**
- additional comparisons with the competing methods in section **D**

A. Proofs of the main results

In this section we provide proofs relative to Algorithm 1, Proposition 2, Proposition 3 and the characterization of the fixed point given by Algorithm 2.

A.1. Global minimum of the hierarchical Gaussian negative log-likelihood

In this section we show that under certain conditions Algorithm 1 actually computes the global minimum of $J_2(\mathbf{x}, \mathbf{z})$ with respect to \mathbf{z} . To reach that conclusion we first decompose the objective function into several terms (equation (22) in proposition 4). Since many of these terms do not depend on \mathbf{z} we conclude that

$$\arg \min_{\mathbf{z}} J_2(\mathbf{x}, \mathbf{z}) = \arg \min_{\mathbf{z}} A(\mathbf{z}) + B(\mathbf{z}).$$

Furthermore, since the second term ($B(\mathbf{z})$) only depends on \mathbf{z} via the determinant of the encoder and decoder covariances, we have that under assumption 1

$$\arg \min_{\mathbf{z}} J_2(\mathbf{x}, \mathbf{z}) = \arg \min_{\mathbf{z}} A(\mathbf{z}).$$

Finally, proposition 5 shows that a functional of the form $A(\mathbf{z})$ reaches its global minimum exactly at the point $E_{\tau}(\mathbf{x})$ computed by Algorithm 1. Hence under assumption 1 we have that

$$\arg \min_{\mathbf{z}} J_2(\mathbf{x}, \mathbf{z}) = \arg \min_{\mathbf{z}} A(\mathbf{z}) = E_{\tau}(\mathbf{x}).$$

Proposition 4 *The objective $J_2(\mathbf{x}, \mathbf{z})$ in equation (17) can be decomposed as*

$$J_2(\mathbf{x}, \mathbf{z}) = f(\mathbf{x}) - \log p_{data}(\mathbf{x}) + A(\mathbf{z}) + B(\mathbf{z}) + C \quad (22)$$

where

$$A(\mathbf{z}) := \sum_{l=0}^{L-1} A_l(\mathbf{z}_l, \mathbf{z}_{<l}) \quad (23)$$

$$B(\mathbf{z}) := \sum_{l=0}^{L-1} B_l(\mathbf{z}_{<l}) \quad (24)$$

$$C := \sum_{l=0}^{L-1} C_l \quad (25)$$

and

$$A_l(\mathbf{z}_l, \mathbf{z}_{<l}) := \|\mathbf{z}_l - m_l(\mathbf{z}_{<l})\|_{S_l^{-1}(\mathbf{z}_{<l})}^2 \quad (26)$$

$$B_l(\mathbf{z}_{<l}) := \frac{1}{2} \log \det(S_l^{-1}(\mathbf{z}_{<l})) + \frac{1}{2} (1 - \lambda_l) \log \det(S_{p,l}^{-1}(\mathbf{z}_{<l})) \quad (27)$$

$$C_l := \frac{d_l}{2} (\log \lambda_l - \lambda_l \log(2\pi)) \quad (28)$$

and

$$m_{p,l}(\mathbf{z}_{<l}) := \mu_{\theta,l}(\mathbf{z}_{<l}) \quad S_{p,l}(\mathbf{z}_{<l}) := \Sigma_{\theta,l}^{-1}(\mathbf{z}_{<l}) \quad (29)$$

$$m_{q,l}(\mathbf{z}_{<l}) := \mu_{\phi,l}(\mathbf{z}_{<l}) \quad S_{q,l}(\mathbf{z}_{<l}) := \Sigma_{\phi,l}^{-1}(\mathbf{z}_{<l}) \quad (30)$$

$$m_l(\mathbf{z}_{<l}) := S_{q,l}(\mathbf{z}_{<l})m_{q,l}(\mathbf{z}_{<l}) + \lambda_l S_{p,l}(\mathbf{z}_{<l})m_{p,l}(\mathbf{z}_{<l}) \quad S_l(\mathbf{z}_{<l}) := S_{q,l}(\mathbf{z}_{<l}) + \lambda_l S_{p,l}(\mathbf{z}_{<l}) \quad (31)$$

Proof. First observe that $q_\phi(\mathbf{z}_l|\mathbf{x}, \mathbf{z}_{<l})$ and $p_\theta(\mathbf{z}_l|\mathbf{z}_{<l})$ are multivariate Gaussians as stated in equation (8). Also $p_\theta(\mathbf{z}_l|\mathbf{z}_{<l})^{\lambda_l}$ behaves like a Gaussian with a different normalization constant, namely

$$p_\theta(\mathbf{z}_l|\mathbf{z}_{<l})^{\lambda_l} = \mathcal{N}(\mathbf{z}_l; m_{p,l}, \lambda_l^{-1} S_{p,l}^{-1}) D_l$$

where the missing normalization constant is

$$D_l = (2\pi)^{-\frac{d_l}{2}(1-\lambda_l)} \lambda_l^{-\frac{d_l}{2}} \det(S_{p,l}^{-1})^{-\frac{1}{2}(1-\lambda_l)}$$

Now $q_\phi(\mathbf{z}_l|\mathbf{x}, \mathbf{z}_{<l})p_\theta(\mathbf{z}_l|\mathbf{z}_{<l})^{\lambda_l}$ is the product of two Gaussians times the correcting term D_l . Since the product of two Gaussians is a Gaussian we obtain

$$q_\phi(\mathbf{z}_l|\mathbf{x}, \mathbf{z}_{<l})p_\theta(\mathbf{z}_l|\mathbf{z}_{<l})^{\lambda_l} = \mathcal{N}(\mathbf{z}_l; m_l, S_l^{-1}) D_l$$

with mean and variance given by equation (31). Taking $-\log$ in the previous expression, we get $A_l + B_l + C_l$ by grouping into A_l the terms depending on both \mathbf{z}_l and $\mathbf{z}_{<l}$, in B_l those depending only on $\mathbf{z}_{<l}$, and into C_l the constant terms. \square

Assumption 1 (Volume-preserving covariances) *The covariance matrices of the HVAE have constant determinant (not depending on $\mathbf{z}_{<l}$, although this constant may depend on the hierarchy level l)*

$$\det(\Sigma_{\phi,l}(\mathbf{z}_{<l}, \mathbf{x})) = c_l(\mathbf{x}) \quad (32)$$

$$\det(\Sigma_{\theta,l}(\mathbf{z}_{<l})) = d_l \quad (33)$$

Proposition 5 (Algorithm 1 computes the global minimum of $J_2(\mathbf{x}, \mathbf{z})$ with respect to \mathbf{z}) *Under Assumption 1 minimizing $J_2(\mathbf{x}, \mathbf{z})$ w.r.t. \mathbf{z} is equivalent to minimizing $A(\mathbf{z})$ defined in equations (23) and (26), i.e.*

$$\arg \min_{\mathbf{z}} J_2(\mathbf{x}, \mathbf{z}) = \arg \min_{\mathbf{z}} A(\mathbf{z}).$$

In addition the global minimum of $A(\mathbf{z}_0, \dots, \mathbf{z}_{L-1})$ is given by the recursion computed by Algorithm 1, namely:

$$\begin{cases} \mathbf{z}_0^* &= m_0 \\ \mathbf{z}_l^* &= m_l(\mathbf{z}_{<l}^*) \text{ for } l \in \{1, \dots, L-1\} \end{cases} \quad (34)$$

where $\mathbf{z}_{<l}^* = (\mathbf{z}_0^*, \dots, \mathbf{z}_{l-1}^*)$, and $m_l(\mathbf{z}_{<l})$ as defined in equations (29) to (31). Put another way, $\mathbf{z}^* = E_\tau(\mathbf{x})$ as computed by Algorithm 1.

Proof. According to the decomposition of J_2 into several terms (equation (22) in proposition 4), we observe that many of these terms do not depend on \mathbf{z} . Therefore we conclude that

$$\arg \min_{\mathbf{z}} J_2(\mathbf{x}, \mathbf{z}) = \arg \min_{\mathbf{z}} A(\mathbf{z}) + B(\mathbf{z}).$$

Furthermore, since the second term ($B(\mathbf{z})$) only depends on \mathbf{z} via the determinant of the encoder and decoder covariances, and these determinants do not depend on \mathbf{z} under assumption 1, we conclude the first part of the proposition, namely

$$\arg \min_{\mathbf{z}} J_2(\mathbf{x}, \mathbf{z}) = \arg \min_{\mathbf{z}} A(\mathbf{z}).$$

Now let's find the global minimum of $A(\mathbf{z})$.

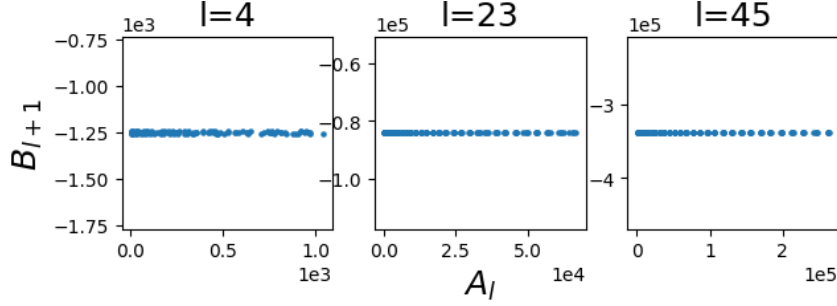


Figure 8: Evolution of $B_{l+1} = \log \det S_{l+1}^{-1}(z_{<l+1})$ as a function of the distance $A_l = \|z_l - \mu_l(z_{<l})\|_{S_l^{-1}(z_{<l})}^2$. (experiment made on VDVAE).

It is clear that $A(z_0, \dots, z_{L-1}) \geq 0$ for all z_0, \dots, z_{L-1} . It is also simple to verify that:

$$\begin{aligned}
 & A(z_1^*, \dots, z_{L-1}^*) \\
 &= \|m_0 - m_0\|_{S_1^{-1}}^2 + \sum_{l=1}^{L-1} \|m_l(z_{<l}^*) - m_l(z_{<l}^*)\|_{S_l^{-1}(z_{<l}^*)}^2 \\
 &= 0.
 \end{aligned} \tag{35}$$

Therefore the minimum value of A is reached in z^* . Furthermore, for any $z \neq z^*$, let us denote by k the first value in $\{0, \dots, L-1\}$ such that $z_k \neq m_k(z_{<k}^*)$. Then,

$$A(z_0, \dots, z_{L-1}) \geq \|z_k - m_k(z_{<k}^*)\|_{S_k^{-1}(z_{<k}^*)}^2 > 0, \tag{36}$$

which implies that z^* is the unique minimum of A . \square

Discussion on assumption 1 (volume preserving covariance) We showed in proposition 5 that, under assumption 1, Algorithm 1 computes the global minimum of $J_2(x, z)$ with respect to z . When optimizing z_l in (22) we only consider the impact of z_l on the distance to the Gaussian mean in $A(z)$, while ignoring its impact on the covariance volumes in the subsequent levels in the terms $B_{l'}(z_{<l'})$, for $l' > l$. If the covariance volumes are constant as stated in assumption 1, the value of z_l has no impact on the covariance volumes of the subsequent levels, and algorithm 1 gives the global minimizer of $J_2(x, \cdot)$ with respect to z . In practice, the HVAE we use does not enforce the covariance matrices of $p(z_l|z_{<l})$ and $q(z_l|z_{<l}, x)$ to have constant volume. However, the experiment in figure 8 shows that the variation of $B_{l+1}(z_{<l+1})$ is negligible in front of $A_l(z_l)$. Hence, we can reasonably expect algorithm 1 to yield the minimum of $J_2(x, z)$ with respect to z . For future works, we could explicitly enforce assumption 1 in the HVAE design.

A.2. Proof of Proposition 2 (Lipschitz constant of one iteration)

Proof. For a decoder with constant covariance $\Sigma_\theta^{-1}(z) = \frac{1}{\gamma^2} \text{Id}$, we have:

$$T(x) = \left(A^t A + \frac{\sigma^2}{\gamma^2} \text{Id} \right)^{-1} \left(A^t y + \frac{\sigma^2}{\gamma^2} \mu_\theta(E_\tau(x)) \right) \tag{37}$$

and then :

$$\|T(u) - T(v)\| \leq \left\| \left(A^t A + \frac{\sigma^2}{\gamma^2} \text{Id} \right)^{-1} \right\| \frac{\sigma^2 L_\tau}{\gamma^2} \|u - v\|. \tag{38}$$

To conclude the proof, we use that for an invertible matrix M , $\|M^{-1}\| = \frac{1}{\sigma_{\min}(M)}$, where $\sigma_{\min}(M)$ is the smallest eigenvalue of M . We also use the fact that α is an eigenvalue of $A^t A + \frac{\sigma^2}{\gamma^2} \text{Id}$ if and only if $\alpha = \lambda + \frac{\sigma^2}{\gamma^2}$ for an eigenvalue $\lambda \geq 0$ of the positive definite matrix $A^t A$. \square

A.3. Proof of Proposition 3 (fixed point of PnP-HVAE)

Proof. \mathbf{x}^* is a fixed point of T if and only if $\mathbf{x}^* = T(\mathbf{x}^*)$. Recalling the definition of $T(\mathbf{x}) := \text{prox}_{\gamma^2 f}(\text{HVAE}(\mathbf{x}, \boldsymbol{\tau}))$, and the definition of proximal operator $\text{prox}_{\gamma^2 f}(\mathbf{x}) = \arg \min_{\mathbf{t}} \gamma^2 f(\mathbf{t}) + \frac{1}{2} \|\mathbf{x} - \mathbf{t}\|^2$, the fixed point condition is equivalent to

$$\mathbf{x}^* = \arg \min_{\mathbf{t}} \frac{1}{2} \|\mathbf{t} - \text{HVAE}(\mathbf{x}^*, \boldsymbol{\tau})\|^2 + \gamma^2 f(\mathbf{t}).$$

Since f is convex the above condition is equivalent to

$$\mathbf{x}^* - \text{HVAE}(\mathbf{x}^*, \boldsymbol{\tau}) + \gamma^2 \nabla f(\mathbf{x}^*) = 0.$$

Rearranging the terms we obtain equation (21). □

Under mild assumptions the above result can be restated as follows: \mathbf{x}^* is a fixed point of T if and only if

$$\nabla f(\mathbf{x}^*) + \nabla g(\mathbf{x}^*) = 0,$$

i.e. whenever \mathbf{x}^* is a *critical point* of the objective function $f(\mathbf{x}) + g(\mathbf{x}) = -\log p(\mathbf{y}|\mathbf{x}) - \log p_{\theta, \boldsymbol{\tau}}(\mathbf{x})$, where the tempered prior is defined as the marginal

$$p_{\theta, \boldsymbol{\tau}}(\mathbf{x}) = \int p_{\theta, \boldsymbol{\tau}}(\mathbf{x}, \mathbf{z}) d\mathbf{z}$$

of the joint tempered prior defined in equation (10).

This is shown in the next section.

A.4. Fixed points are critical points

In this section we characterize fixed points of Algorithm 2 as critical points of a posterior density (a necessary condition to be a MAP estimator), under mild conditions. Before we formulate this characterization we need to review in more detail a few facts about HVAE training, temperature scaling and our optimization model.

HVAE training. In section 3.1 we introduced how VAEs in general (and HVAEs in particular) are trained. As a consequence an HVAE embeds a joint prior

$$p_{\theta}(\mathbf{x}, \mathbf{z}) := p_{\theta}(\mathbf{x}|\mathbf{z})p_{\theta}(\mathbf{z}) \tag{39}$$

from which we can define a marginal prior on \mathbf{x}

$$p_{\theta}(\mathbf{x}) := \int p_{\theta}(\mathbf{x}, \mathbf{z}) d\mathbf{z}. \tag{40}$$

In addition, from the ELBO maximization condition in (5) and Bayes theorem we can obtain an alternative expression for the joint prior, namely

$$p_{\theta}(\mathbf{x}, \mathbf{z}) = q_{\phi}(\mathbf{z}|\mathbf{x})p_{\text{data}}(\mathbf{x}). \tag{41}$$

Temperature scaling. After training we reduce the temperature by a factor $\boldsymbol{\tau}$, which amounts to replacing $p_{\theta}(\mathbf{z})$ by

$$p_{\theta, \boldsymbol{\tau}}(\mathbf{z}) := \prod_{l=0}^{L-1} \frac{p_{\theta}(\mathbf{z}_l | \mathbf{z}_{<l})^{\frac{1}{\tau_l}}}{Z_l}$$

as shown in equation (10), leading to the joint tempered prior

$$p_{\theta, \boldsymbol{\tau}}(\mathbf{x}, \mathbf{z}) := p_{\theta}(\mathbf{x}|\mathbf{z})p_{\theta, \boldsymbol{\tau}}(\mathbf{z}). \tag{42}$$

The corresponding marginal tempered prior on \mathbf{x} becomes

$$p_{\theta, \boldsymbol{\tau}}(\mathbf{x}) := \int p_{\theta, \boldsymbol{\tau}}(\mathbf{x}, \mathbf{z}) d\mathbf{z} \tag{43}$$

and the corresponding posterior is

$$p_{\theta, \boldsymbol{\tau}}(\mathbf{z}|\mathbf{x}) := p_{\theta, \boldsymbol{\tau}}(\mathbf{x}, \mathbf{z})/p_{\theta, \boldsymbol{\tau}}(\mathbf{x}). \tag{44}$$

The joint tempered prior also has an alternative expression (based on the encoder). Indeed substituting $p_\theta(\mathbf{x}|\mathbf{z})$ from equations (39) and (41) into (42) we obtain

$$p_{\theta,\tau}(\mathbf{x}, \mathbf{z}) = \frac{p_{\theta,\tau}(\mathbf{z})}{p_\theta(\mathbf{z})} q_\phi(\mathbf{z}|\mathbf{x}) p_{\text{data}}(\mathbf{x}). \quad (45)$$

Substituting this result into definition (44) we obtain an alternative expression for the tempered posterior

$$p_{\theta,\tau}(\mathbf{z}|\mathbf{x}) = q_\phi(\mathbf{z}|\mathbf{x}) p_{\text{data}}(\mathbf{x}) / p_\theta(\mathbf{z}). \quad (46)$$

Optimization model. Since we are using a scaled prior $p_{\theta,\tau}(\mathbf{x})$ encoded in our HVAE to regularize the inverse problem, the ideal optimization objective we would like to minimize is

$$U(\mathbf{x}) := \underbrace{-\log p(\mathbf{y}|\mathbf{x})}_{f(\mathbf{x})} - \underbrace{\log p_{\theta,\tau}(\mathbf{x})}_{g(\mathbf{x})}. \quad (47)$$

Since $p_{\theta,\tau}(\mathbf{x})$ is intractable our algorithm seeks to minimize a relaxed objective (see equation (15)). Nevertheless, under certain conditions (to be specified below) this is equivalent to minimizing the ideal objective (47).

Fixed-point characterization. We start by characterizing $\nabla \log p_{\theta,\tau}(\mathbf{x})$ in terms of an HVAE-related denoiser (Proposition 6). Then we relate this denoiser to the quantity $\text{HVAE}(\mathbf{x}, \tau)$ that is computed by our algorithm (Proposition 7). As a consequence we obtain that the fixed point condition in Proposition 3 can be written as $\nabla U(\mathbf{x}) = 0$ (see Corollary 2).

Proposition 6 (Tweedie's formula for HVAEs.) *For an HVAE with Gaussian decoder $p_\theta(\mathbf{x}|\mathbf{z}) = \mathcal{N}(\mathbf{x}; \mu_\theta(\mathbf{z}), \gamma^2 I)$, the following denoiser based on the HVAE with tempered prior*

$$D_{\theta,\tau}(\mathbf{x}) := \int \mu_\theta(\mathbf{z}) p_{\theta,\tau}(\mathbf{z}|\mathbf{x}) d\mathbf{z} \quad (48)$$

satisfies Tweedie's formula

$$D_{\theta,\tau}(\mathbf{x}) - \mathbf{x} = \gamma^2 \nabla \log p_{\theta,\tau}(\mathbf{x}) = -\gamma^2 \nabla g(\mathbf{x}). \quad (49)$$

Proof. From the definition of $p_{\theta,\tau}(\mathbf{x})$ in equation (43) we have that

$$\nabla \log p_{\theta,\tau}(\mathbf{x}) = \frac{1}{p_{\theta,\tau}(\mathbf{x})} \int \nabla_{\mathbf{x}} p_\theta(\mathbf{x}|\mathbf{z}) p_{\theta,\tau}(\mathbf{z}) d\mathbf{z}.$$

From the pdf of the Gaussian decoder $p_\theta(\mathbf{x}|\mathbf{z})$ its gradient writes

$$\nabla_{\mathbf{x}} p_\theta(\mathbf{x}|\mathbf{z}) = -\frac{1}{\gamma^2} (\mathbf{x} - \mu_\theta(\mathbf{z})) p_\theta(\mathbf{x}|\mathbf{z}).$$

Replacing this in the previous equation we get

$$\begin{aligned} \nabla \log p_{\theta,\tau}(\mathbf{x}) &= \frac{1}{\gamma^2} \int (\mu_\theta(\mathbf{z}) - \mathbf{x}) \frac{p_\theta(\mathbf{x}|\mathbf{z}) p_{\theta,\tau}(\mathbf{z})}{p_{\theta,\tau}(\mathbf{x})} d\mathbf{z} \\ &= \frac{1}{\gamma^2} \int (\mu_\theta(\mathbf{z}) - \mathbf{x}) p_{\theta,\tau}(\mathbf{z}|\mathbf{x}) d\mathbf{z} \\ &= \frac{1}{\gamma^2} \left(\int \mu_\theta(\mathbf{z}) p_{\theta,\tau}(\mathbf{z}|\mathbf{x}) d\mathbf{z} - \mathbf{x} \right). \end{aligned}$$

In the second step we used the definitions of the joint tempered prior $p_{\theta,\tau}(\mathbf{x}, \mathbf{z})$ (42) and the tempered posterior $p_{\theta,\tau}(\mathbf{z}|\mathbf{x})$ (44). The last step follows from the fact that $\int p_{\theta,\tau}(\mathbf{z}|\mathbf{x}) d\mathbf{z} = 1$ according to definitions (44) and (43). Finally applying the definition of the denoiser $D_{\theta,\tau}(\mathbf{x})$ in the last expression we obtain Tweedie's formula (49). \square

Under suitable assumptions the denoiser defined above coincides with $\text{HVAE}(\mathbf{x}, \tau)$ computed by our algorithm.

Assumption 2 (Deterministic encoder) The covariance matrices of the encoder defined in equation (8) are 0, i.e. $\Sigma_{\phi,l}(\mathbf{z}_{<l}, \mathbf{x}) = 0$ for $l = 0, \dots, L - 1$. Put another way $q_{\phi}(\mathbf{z}|\mathbf{x}) = \delta_{E_{\tau}(\mathbf{x})}(\mathbf{z})$ is a Dirac centered at $E_{\tau}(\mathbf{x})$.

Proposition 7 Under Assumption 2 the function $\text{HVAE}(\mathbf{x}, \tau)$ computed by Algorithm 2 coincides with the denoiser $D_{\theta, \tau}(\mathbf{x})$ defined in equation (48).

Proof. $\text{HVAE}(\mathbf{x}, \tau)$ is defined in Proposition 3 as

$$\text{HVAE}(\mathbf{x}, \tau) = \mu_{\theta}(E_{\tau}(\mathbf{x})).$$

First observe that for a deterministic encoder we also have $p_{\theta, \tau}(\mathbf{z}|\mathbf{x}) = \delta_{E_{\tau}(\mathbf{x})}(\mathbf{z})$. Indeed for any test function h :

$$\begin{aligned} \int h(\mathbf{z}) p_{\theta, \tau}(\mathbf{z}|\mathbf{x}) d\mathbf{z} &= \int h(\mathbf{z}) q_{\phi}(\mathbf{z}|\mathbf{x}) p_{\text{data}}(\mathbf{x}) / p_{\theta}(\mathbf{z}) d\mathbf{z} \\ &= h(E_{\tau}(\mathbf{x})) \underbrace{p_{\text{data}}(\mathbf{x}) / p_{\theta}(E_{\tau}(\mathbf{x}))}_{Z(\mathbf{x})}. \end{aligned}$$

And the normalization constant $Z(\mathbf{x})$ should be equal to 1 because $\int p_{\theta, \tau}(\mathbf{z}|\mathbf{x}) d\mathbf{z} = Z(\mathbf{x}) = 1$. Hence $p_{\theta, \tau}(\mathbf{z}|\mathbf{x}) = q_{\phi}(\mathbf{z}|\mathbf{x}) = \delta_{E_{\tau}(\mathbf{x})}(\mathbf{z})$.

Finally applying the definition of $D_{\theta, \tau}(\mathbf{x})$ we obtain

$$\begin{aligned} D_{\theta, \tau}(\mathbf{x}) &= \int \mu_{\theta}(\mathbf{z}) p_{\theta, \tau}(\mathbf{z}|\mathbf{x}) d\mathbf{z} = \mu_{\theta}(E_{\tau}(\mathbf{x})) \\ &= \text{HVAE}(\mathbf{x}, \tau). \end{aligned}$$

□

Combining Propositions 7, 3 and 6 we obtain a new characterization of fixed points as critical points.

Corollary 2 Under Assumption 2 \mathbf{x}^* is a fixed point of T if and only if

$$\nabla f(\mathbf{x}^*) + \nabla g(\mathbf{x}^*) = 0 \quad (50)$$

where $g(\mathbf{x}) = -\log p_{\theta, \tau}(\mathbf{x})$.

Proof. From Proposition 6 we have that

$$-\nabla g(\mathbf{x}) = \frac{1}{\gamma^2} (D_{\theta, \tau}(\mathbf{x}) - \mathbf{x}).$$

From Proposition 7 we have that (under Assumption 2) $D_{\theta, \tau}(\mathbf{x}) = \text{HVAE}(\mathbf{x}, \tau)$. In combination with the previous result:

$$-\nabla g(\mathbf{x}) = \frac{1}{\gamma^2} (\text{HVAE}(\mathbf{x}, \tau) - \mathbf{x}).$$

Finally, Proposition 3 allows to conclude that

$$-\nabla g(\mathbf{x}) = \nabla f(\mathbf{x}).$$

□

B. Details on PatchVDVAE architecture

In this section, we provide additional details about the architecture of PatchVDVAE. Then, we present the choice of the hyperparameters used for the concurrent methods (presented in section 6 of the main paper).

B.1. PatchVDVAE

Figure 9 provides a detailed overview of the structure of a PatchVDVAE network. The architecture follows VDAE model [6], except for the first top-down block, in which we replace the constant input by a latent variable sampled from a Gaussian distribution. The architecture presented in figure 9 illustrates the structure of HVAE networks, but the number of blocks is different to the PatchVDVAE network used in our experiments. Our PatchVDVAE top-down path is composed of $L = 30$ top-down blocks of increasing resolution. The image features are upsampled using an unpooling layer every 5 blocks. The first unpooling layer performs a $\times 4$ upsampling, and the following unpooling layers perform $\times 2$ upsampling. The dimension of the filters is 256 in all blocks. In order to save computations in the residual blocks, the 3×3 convolutions are applied on features of reduced channel dimension (divided by 4). 1×1 convolutions are applied before and after the 3×3 convolutions to respectively reduce and increase the number of channels. The latent variables z_l are tensors of shape $12 \times H_l \times W_l$, where the resolution H_l, W_l corresponds to the resolution of the corresponding top-down-block. The bottom-up network structure is symmetric to the top-down network, with 5 residual blocks for each scale, and pooling layers between each scale.

B.2. Hyperparameters of compared methods

Face image restoration. For ILO, we found that optimizing the first 5 layers of the generative network offered the best trade-off between image quality and consistency with the observation. Hence, we optimize the 5 first layers for 100 iterations each. This choice is different from the official implementation, where they only optimize the 4 first layers for a lower number of iterations, trading restoration performance for speed. For DPS, we set the scale hyper-parameter ζ' (described in subsection C.2 in [7]) to $\zeta' = 1$ for the deblurring and super-resolution experiments reported in this paper.

Natural images restoration - Deblurring. For the three tested methods, we use the official implementation provided by the authors, along with the pretrained models. For EPLL, we use the default parameters in the official implementation.

For GS-PnP, using the notation of the paper, we use the suggested hyperparameter $\lambda_\nu = 0.1$ for the motion blur kernels and $\lambda_\nu = 0.75$ for the Gaussian kernels.

For PnP-MMO, we use the denoiser trained on $\sigma_{den} = 0.007$. On deblurring with $\sigma = 2.55$ we use the default parameters in the implementation. for higher noise levels ($\sigma = 7.65$; $\sigma = 12.75$), and we set the strength of the gradient step as $\gamma = \sigma_{den} / (2\sigma \|h\|)$, where h corresponds to the blur kernel.

Natural images restoration- Inpainting. For EPLL, we use the default parameters provided in the authors matlab code. For GS-PnP, after a grid-search, we chose to set $\lambda_\nu = 1$ and $\sigma_{denoiser} = 10$.

C. Discussion on the contractivity of HVAE

We showed in section 5 that PnP-HVAE converges to a fixed point under the assumption that $x \rightarrow HVAE(x, \tau)$ is contractive. If this condition is met, the sequence of u_k defined by $u_{k+1} = HVAE(u_k, \tau)$ should converge to a fixed point. Figure 10 presents the **evolution of a fixed point iteration** $u_{k+1} = HVAE(u_k, \tau)$. The image is smoothened over the iterations, and finally converges to a piecewise constant image. We used patchVDVAE for this experiment.

D. Comparisons

In this section, we provide additional visual results on face images and natural images.

D.1. Additional results on face image restoration

We provide additional comparisons with the GAN-based ILO method on inpainting (figure 11), $\times 4$ super-resolution (figure 12) and deblurring (figure 13). PnP-HVAE provides equally or more plausible glasses in the first column) inpainting than ILO. For superresolution, ILO produces sharper but not realistic faces. This is an agreement with the scores presented in table 1). For deblurring, ILO creates textures on faces that looks realistic (low LPIPS) but are less consistent with the observation (significantly lower PSNR and SSIM).

D.2. Additional results on natural images restoration

We finally present additional results on natural images restoration. All the PnP-HVAE images presented below were produced using our PatchVDVAE model. We also provide visual comparisons with concurrent PnP methods and EPLL. For

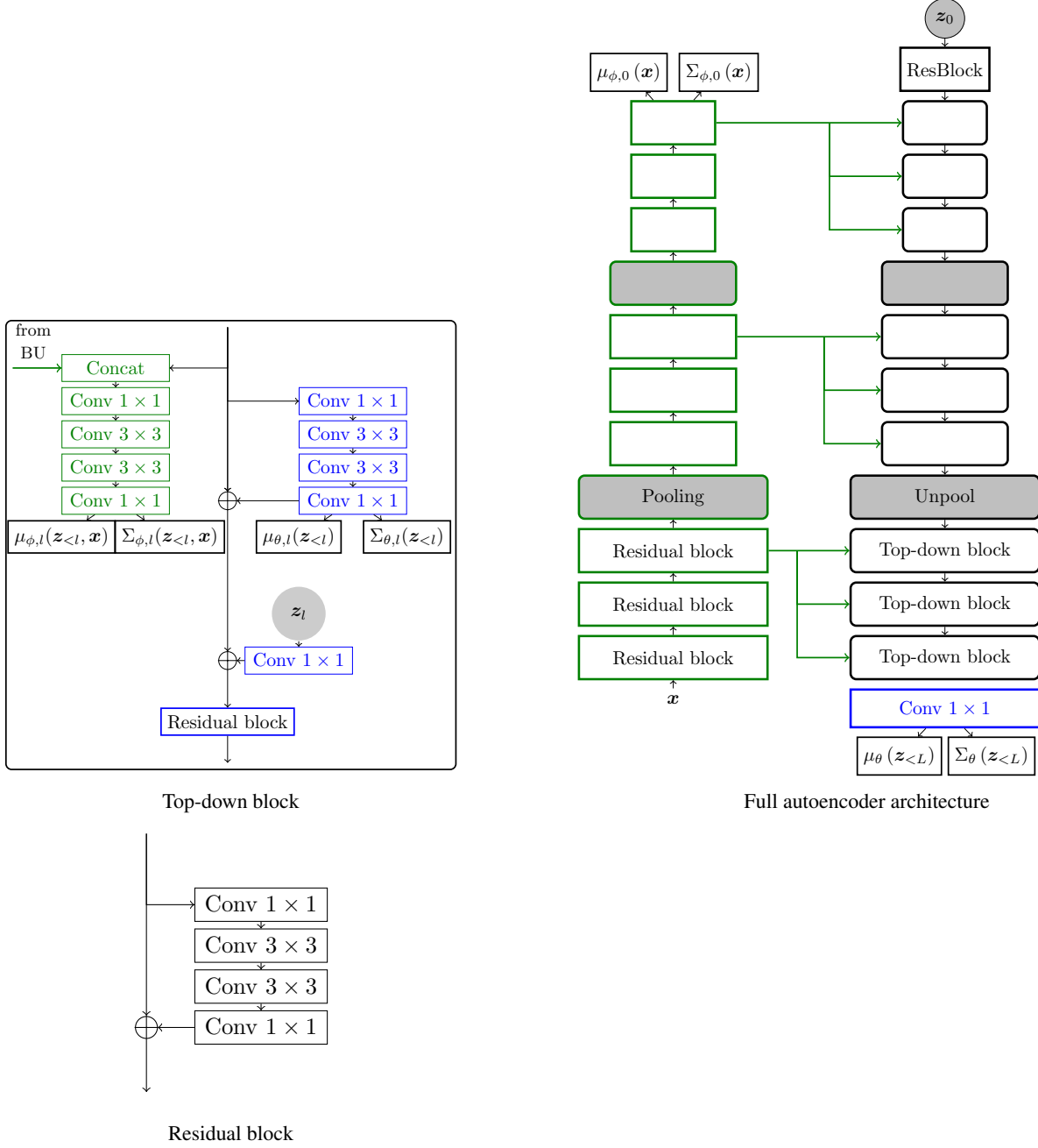


Figure 9: Structure of the PatchVDVAE architecture. For clarity, we omit the non-linearity after each convolution.

deblurring (figures 15 and 16, PnP methods perform better than EPLL. Following quantitative results of figure 2, for larger noise level, PnP-HVAE outperforms PnP-MMO and provides restoration close to GS-PnP.

For inpainting (figure 17), the hierarchical structure of PatchVDVAE leads to more plausible reconstructions, and PnP-HVAE outperforms the compared methods.

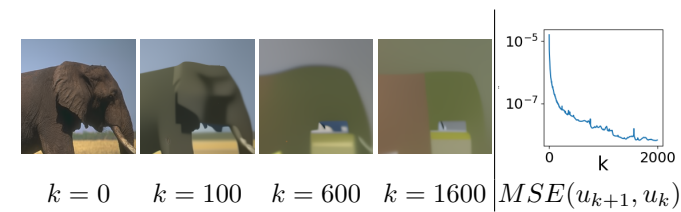


Figure 10: Fixed-point iterations of patchVDVAE for $\tau = 0.99$.

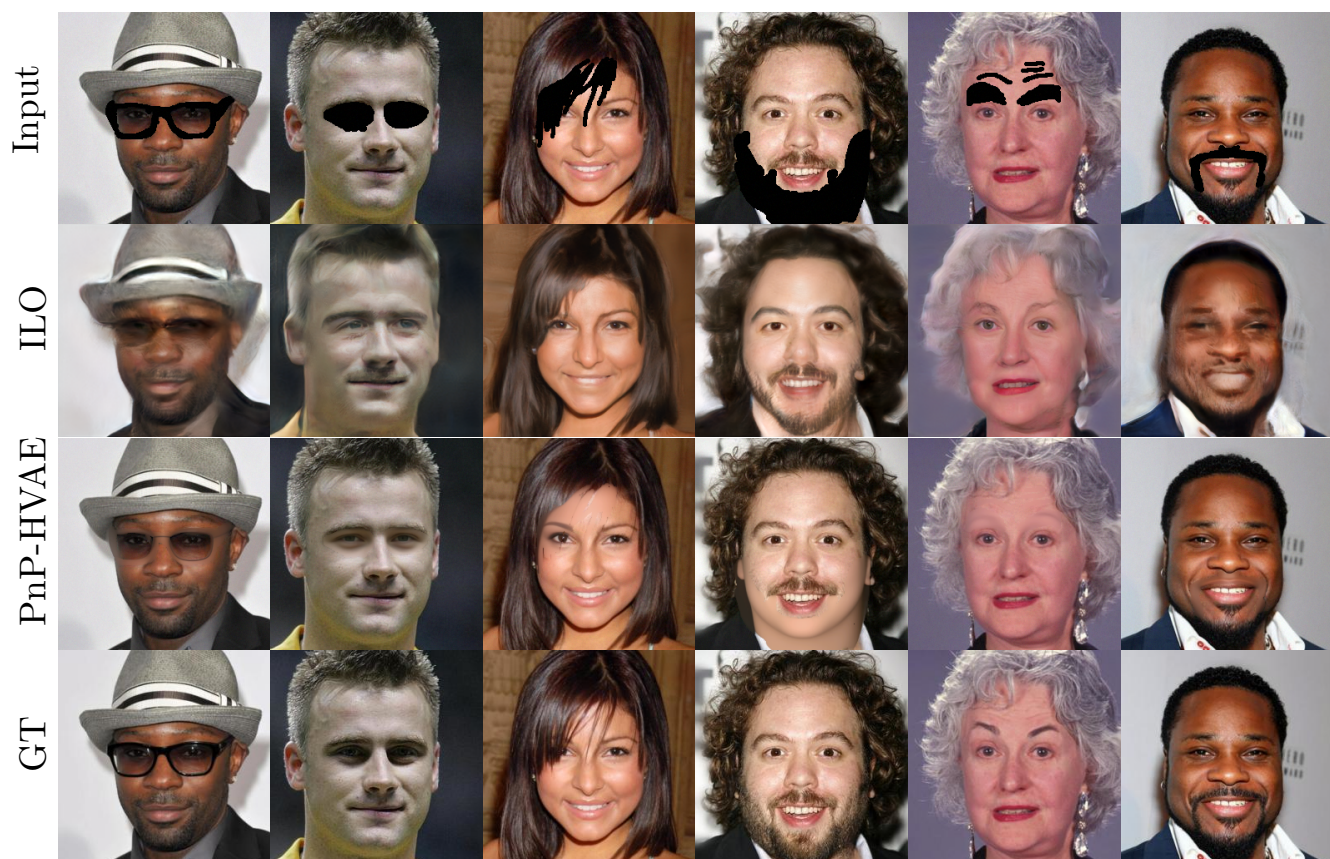


Figure 11: Inpainting



Figure 12: $\times 4$ super-resolution, with kernel (a) from Figure 14 and $\sigma = 3$

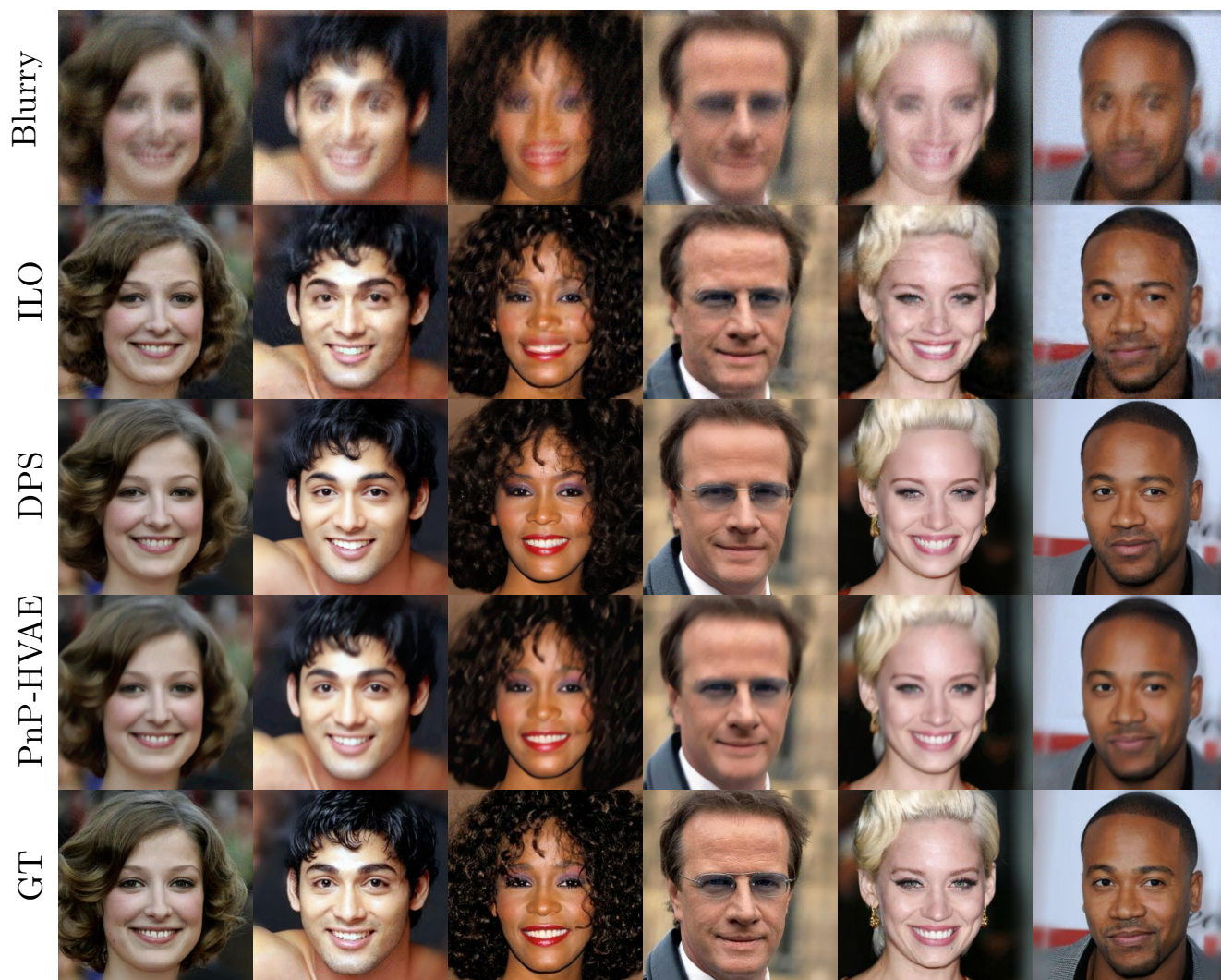


Figure 13: Deblurring, with kernel (d) from Figure 14 and $\sigma = 8$

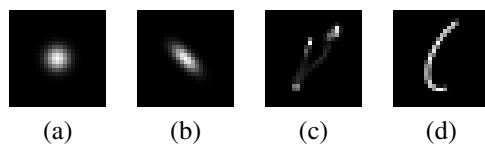
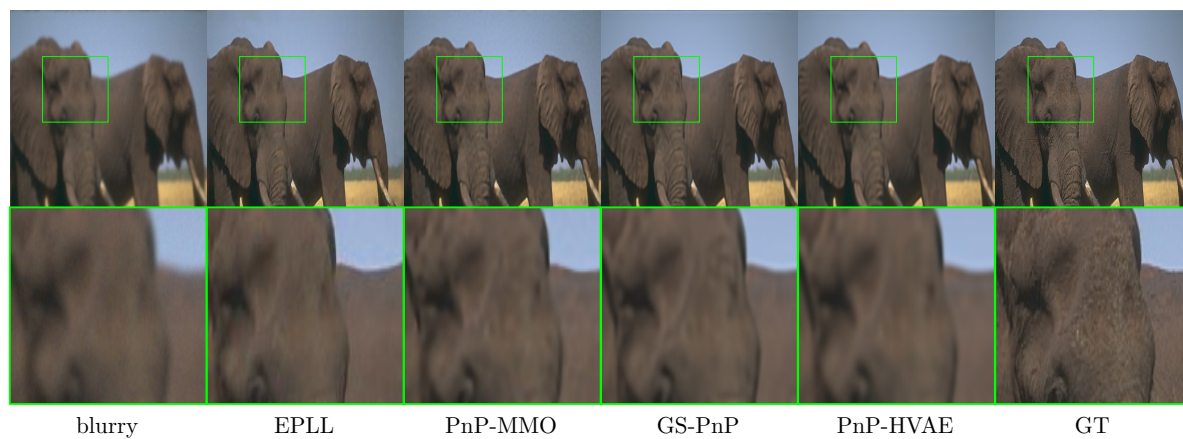


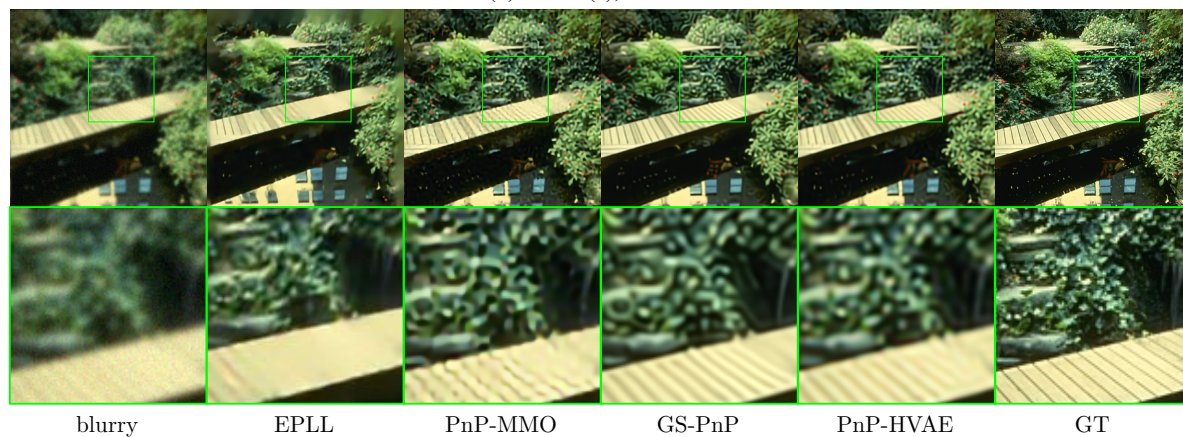
Figure 14: Kernels used for deblurring experiments, from [27]



(a) kernel (a), $\sigma = 2.55$

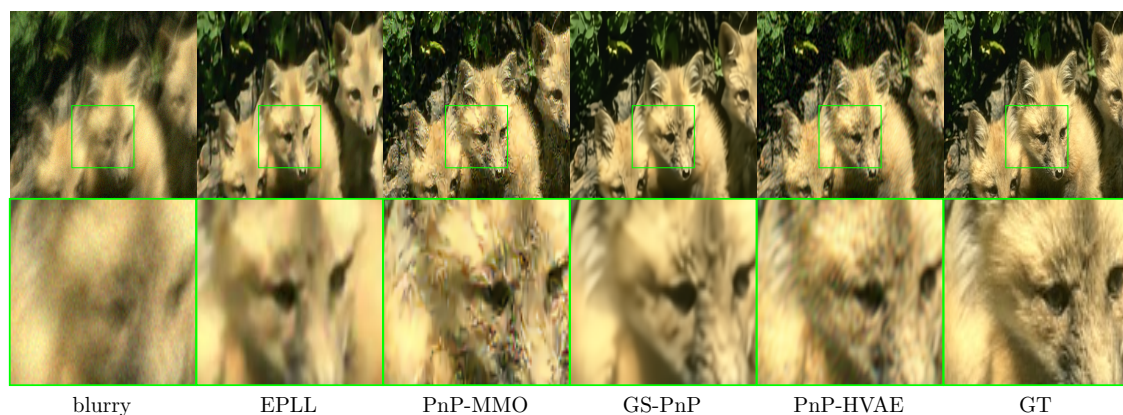


(b) kernel (c), $\sigma = 2.55$

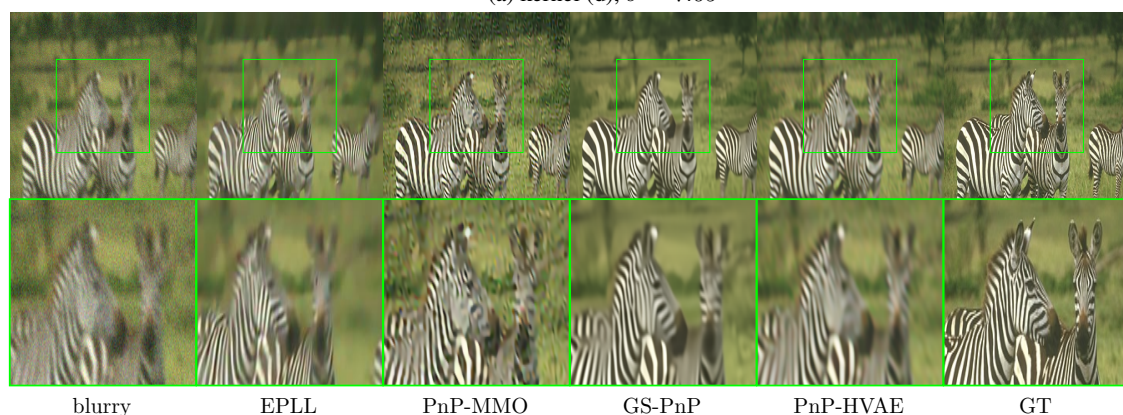


(c) kernel (a), $\sigma = 7.65$

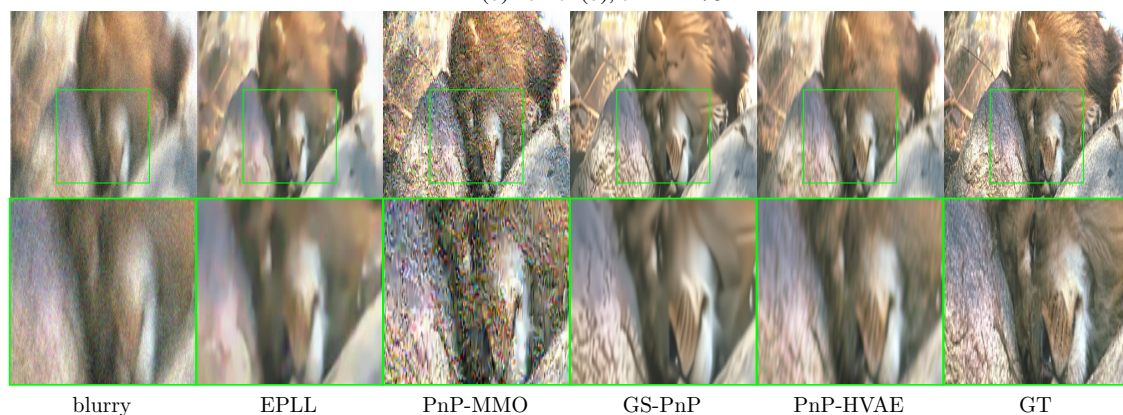
Figure 15: Deblurring results on BSD



(a) kernel (d), $\sigma = 7.65$



(b) kernel (b), $\sigma = 12.75$



(c) kernel (d), $\sigma = 12.75$

Figure 16: Deblurring results on BSD

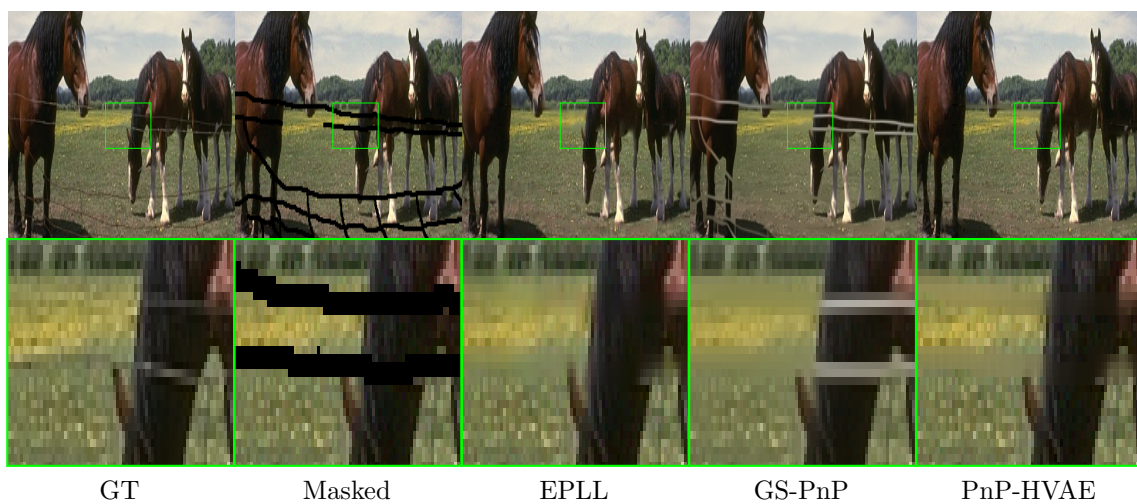


Figure 17: Natural images inpainting